Atmospheric
Chemistry
and Physics
Discussions

Open Access

EGU

Precipitation Susceptibility of Marine Stratocumulus with Variable Above and Below-Cloud Aerosol Concentrations over the Southeast Atlantic

Siddhant Gupta[1,2], Greg M. McFarquhar[1,2], Joseph R. O'Brien[3], Michael R. Poellot[3], David J. Delene[3], Rose M. Miller[4], and Jennifer D. Small Griswold[5]

5   [1]Cooperative Institute for Mesoscale Meteorological Studies, University of Oklahoma, Norman, OK, USA
[2]School of Meteorology, University of Oklahoma, Norman, OK, USA
[3]Department of Atmospheric Sciences, University of North Dakota, Grand Forks, ND, USA
[4]Department of Atmospheric Sciences, University of Illinois at Urbana-Champaign, Urbana, IL,
10   USA
[5]Department of Meteorology, University of Hawai'i at Manoa, Honolulu, HI, USA

Correspondence to: Siddhant Gupta (sid@ou.edu)

Abstract. Aerosol-cloud-precipitation interactions (ACIs) provide the greatest source of

15   uncertainties in predicting changes in Earth's energy budget due to poor representation of

marine stratocumulus and the associated ACIs in climate models. Using in situ data from 329

cloud profiles across 24 research flights from the NASA ObseRvations of Aerosols above CLouds

and their intEractionS (ORACLES) field campaign in September 2016, August 2017, and October

2018, it is shown that contact between above-cloud biomass-burning aerosols and marine

20   stratocumulus over the southeast Atlantic Ocean was associated with precipitation suppression

and a decrease in the precipitation susceptibility (S_o) to aerosols. The 173 "contact" profiles with

aerosol concentration (N_a) greater than 500 cm^{-3} within 100 m above cloud tops had 50 % lower

precipitation rate (R_p) and 20 % lower S_o, on average, compared to 156 "separated" profiles with

N_a less than 500 cm^{-3} up to at least 100 m above cloud tops.

25   Contact and separated profiles had statistically significant differences in droplet

concentration (N_c) and effective radius (R_e) (95 % confidence intervals from a two-sample t-test

are reported). Contact profiles had 84 to 90 cm^{-3} higher N_c and 1.4 to 1.6 μm lower R_e compared

to separated profiles. In clean boundary layers (below-cloud N_a less than 350 cm^{-3}), contact profiles had 25 to 31 cm^{-3} higher N_c and 0.2 to 0.5 μm lower R_e. In polluted boundary layers

30   (below-cloud N_a exceeding 350 cm^{-3}), contact profiles had 98 to 108 cm^{-3} higher N_c and 1.6 to 1.8 μm lower R_e. On the other hand, contact and separated profiles had statistically insignificant differences between the average liquid water path, cloud thickness, and meteorological parameters like surface temperature, lower tropospheric stability, and estimated inversion strength. These results suggest the changes in cloud properties were driven by ACIs rather than

35   meteorological effects, and the existing relationships between R_p and N_c must be adjusted to account for the role of ACIs.

1 Introduction

Clouds drive the global hydrological cycle with an annual average precipitation rate of 3 mm day^{-1} over the oceans (Behrangi et al., 2014). Marine stratocumulus (MSC) is the most

40   common cloud type with an annual coverage of 22 % over the ocean surface (Eastman et al., 2011). These low-level, boundary layer clouds typically exist over subtropical oceans in regions with large-scale subsidence such as the southeast Atlantic Ocean (Klein and Hartmann, 1993). MSC have higher reflectivity (albedo) than the ocean surface which results in a strong, negative shortwave cloud radiative forcing (CRF) with a weak and positive longwave CRF (Oreopoulos and

45   Rossow, 2011).

Low-cloud cover in the subsidence regions is negatively correlated with sea surface temperature (SST) (Eastman et al., 2011; Wood and Hartmann, 2006). CRF is thus sensitive to changes in SST but there is a large spread in model estimates of CRF sensitivity (Bony and

Dufresne, 2005). This provides uncertainty in the model estimates of Earth's energy budget in

50   future climate scenarios (Trenberth and Fasullo, 2009). Uncertainty in parameterization of

boundary layer aerosol, cloud, and precipitation processes contributes to model uncertainties

(Ahlgrimm and Forbes, 2014; Stephens et al., 2010).

MSC CRF is regulated by cloud processes that depend on cloud microphysical properties,

like droplet concentration (N_c), effective radius (R_e), and liquid water content (LWC), and

55   macrophysical properties, like cloud thickness (H) and liquid water path (LWP). These cloud

properties can depend on the concentration, composition, and size distributions of aerosols

which act as cloud condensation nuclei. Under conditions of constant LWC, increases in aerosol

concentration (N_a) can increase N_c and decrease R_e, strengthening the shortwave CRF (Twomey,

1974, 1977). A decrease in droplet sizes in polluted clouds can inhibit droplet growth from

60   collision-coalescence and suppress precipitation intensity, resulting in lower precipitation rate

(R_p), higher LWP, and increased cloud lifetime (Albrecht, 1989). In combination, these aerosol-

cloud-precipitation interactions (ACIs) and the resulting cloud adjustments lead to an effective

radiative forcing termed ERF$_{aci}$ (Boucher et al., 2013).

Satellite retrievals of R_e and cloud optical thickness (τ) can be used to estimate N_c and

65   LWP using the adiabatic assumption (Boers et al., 2006; Wood and Hartmann, 2006; Bennartz,

2007). LWC increases linearly with height in adiabatic clouds and τ is parameterized as a function

of N_c and LWP ($\tau \propto N_c^{1/3}$ LWP$^{5/6}$) (Brenguier et al., 2000). Since τ has greater sensitivity to LWP

compared to N_c, assuming constant LWP can lead to underestimation of the cloud albedo

susceptibility to aerosol perturbations (Platnick and Twomey, 1994).

Atmospheric
Chemistry
and Physics
Discussions

Open Access

EGU

70   LWP can have a positive or negative response to increasing N_c due to aerosols (Toll et al.,

2019). The LWP response is regulated by environmental conditions (e.g., lower tropospheric

stability (LTS), boundary layer depth (H_{BL}), and relative humidity), cloud particle sizes (e.g.,

represented by R_e), R_p, and by N_c and LWP themselves (Chen et al., 2014; Gryspeerdt et al., 2019;

Toll et al., 2019; Possner et al., 2020). Accurate estimation of the LWP response to aerosol

75   perturbations is important for regional and global estimates of ERF$_{aci}$ (Douglas and L'Ecuyer,

2019; 2020).

Droplet evaporation associated with cloud-top entrainment and precipitation are the two

major sinks of LWP in MSC. Smaller droplets associated with higher N_c or N_a evaporate more

readily which leads to greater cloud-top evaporative cooling and a negative LWP response (Hill

80   et al., 2008). The LWP response to the evaporation-entrainment feedback (Xue and Feingold,

2006; Small et al., 2009) also depends on above-cloud humidity (Ackerman et al., 2004).

Precipitation susceptibility (S_o) to aerosol-induced changes in cloud properties is defined as the

change in R_p due to aerosol-induced changes in N_c and is a function of LWP or H (Feingold and

Seibert, 2009).

85   The magnitude of S_o depends on precipitation formation processes like collision-

coalescence which are parameterized using mass transfer rates, such as the autoconversion rate

(S_{AUTO}) and the accretion rate (S_{ACC}) (Morrison and Gettelman, 2008; Geoffroy et al., 2010).

Autoconversion describes the process of collisions between cloud droplets that coalesce to form

drizzle drops which initiate precipitation. Accretion refers to collisions between cloud droplets

90   and drizzle drops which lead to larger drizzle drops and greater precipitation intensity. The

Atmospheric
Chemistry
and Physics
Discussions

variability in S_o as a function of LWP or H depends on the cloud type and the ratio of S_{ACC} versus S_{AUTO} (Wood et al., 2009; Jiang et al., 2010; Sorooshian et al., 2010).

Recent studies of ACIs have focused on the southeast Atlantic Ocean because of the unique meteorological conditions present in the region (Zuidema et al., 2016; Redemann et al.,

95   2021). Biomass-burning aerosols from southern Africa are transported over an extensive MSC deck that exists off the coast of Namibia and Angola (Adebiyi and Zuidema, 2016; Devasthale and Thomas, 2011). The aerosol layer is comprised of shortwave-absorbing aerosols (500 nm single-scattering albedo of about 0.83) and high above-cloud aerosol optical depth (up to 0.42) (Pistone et al., 2019; LeBlanc et al., 2020). The sign of the forcing due to shortwave absorption by the

100   aerosol layer depends on the location of aerosols in the vertical column and the albedo of the underlying clouds (Cochrane et al., 2019).

Satellite retrievals suggest warming aloft due to a positive forcing decreases dry air entrainment into clouds, increases LWP and cloud albedo, and decreases the shortwave CRF (Wilcox, 2010). The net radiative forcing due to the aerosol and cloud layers thus depends on

105   aerosol-induced changes in N_c, R_e, and LWP and the resulting changes in τ. Sinks of N_c and LWP like precipitation and entrainment mixing lead to uncertainties in satellite retrievals of N_c which pose the biggest challenge in the use of satellite retrievals to study the aerosol impact on N_c (Quaas et al., 2020). This motivates observational studies of ACIs that examine N_c and LWP under different aerosol and meteorological conditions.

110   In situ observations of cloud and aerosol properties were collected over the southeast Atlantic during the NASA ObseRvations of Aerosols above CLouds and their intEractionS

(ORACLES) field campaign during three Intensive Observation Periods (IOPs) in September 2016, August 2017, and October 2018 (Redemann et al., 2021). The above-cloud aerosol plume was associated with elevated water vapor content (Pistone at al., 2021) which influenced cloud-top

115   humidity and dynamics following the mechanisms discussed by Ackerman et al. (2004).

During the 2016 IOP, variable vertical displacement (0 to 2000 m) was observed between above-cloud aerosols and the MSC (Gupta et al., 2021; hereafter G21). Instances of contact and separation between the aerosol and cloud layers were associated with differences in the above- and below-cloud N_a, water vapor mixing ratio (w_v), and cloud-top entrainment processes. These

120   differences led to changes in N_c, R_e, and LWC, and their vertical profiles (G21). In this study, the response of the MSC to above- and below-cloud aerosols is further examined using data from all three ORACLES IOPs, and precipitation formation and S_o are evaluated as a function of H.

The paper is organized as follows. In Section 2, the ORACLES observations are discussed along with the data quality assurance procedures (additional details are in a supplement). In

125   Section 3, the calculation of cloud properties is described. In Section 4, the influence of aerosols on N_c, R_e, and LWC is examined by comparing the parameters for MSC in contact or separated from the above-cloud aerosol layer. In Section 5, the changes in precipitation formation due to aerosol-induced microphysical changes are examined. In Section 6, N_c, R_p, and S_o are examined as a function of H and the above- and below-cloud N_a. In Section 7, the meteorological conditions

130   are examined using reanalysis data. In Section 8, the conclusions are summarized with directions for future work.

2 Observations

The ORACLES IOPs were based at Walvis Bay, Namibia (23° S, 14.6° E) in September 2016,

135 and at São Tomé and Príncipe (0.3° N, 6.7° E) in August 2017 and October 2018. The data analyzed

in this study were collected during the three IOPs (Table 1 and Figure 1): six P-3 research flights

(PRFs) from 6 to 25 September 2016 with cloud sampling conducted between 1° W to 12° E and

9° S to 20° S; seven PRFs from 12 to 28 August 2017 with cloud sampling conducted between 8°

W to 6° E and 2° S to 15° S; and 11 PRFs from 27 September to 23 October 2018 with cloud

140 sampling conducted between 3° W to 9° E and 1° N to 15° S. These PRFs were selected because

in situ cloud sampling was conducted during at least three vertical profiles through the cloud

layer (Table 1).

Three PRFs from the 2016 IOP had overlapping tracks when the P-3B aircraft flew north-

west from 23° S, 13.5° E toward 10° S, 0° E, and returned along the same track (Figure 1). The

145 2017 and 2018 IOPs had 10 PRFs with overlapping flight tracks when the aircraft flew south from

0° N, 5° E toward 15° S, 5° E, and returned along the same track. PRFs with overlapping tracks

acquired statistics for model evaluation (Doherty et al., 2021) while the other PRFs targeted

specific locations based on meteorological conditions (Redemann et al., 2021).

During ORACLES, the NASA P-3B aircraft was equipped with in situ probes. The data

150 analyzed in this study were collected using Cloud Droplet Probes (CDPs), a Cloud and Aerosol

Spectrometer (CAS) on the Cloud, Aerosol and Precipitation Spectrometer, a Phase Doppler

Interferometer (PDI), a Two-Dimensional Stereo Probe (2D-S), a High Volume Precipitation

Sampler (HVPS-3), a King hot-wire, and a Passive Cavity Aerosol Spectrometer Probe (PCASP). A

Atmospheric
Chemistry
and Physics
Discussions

single CDP was used during the 2016 IOP (hereafter CDP-A), a second CDP (hereafter CDP-B) was

155   added for the 2017 and 2018 IOPs, and CDP-A was replaced by a different CDP (hereafter CDP-C)

for the 2018 IOP.

The CAS, CDP, King hot-wire, and PCASP data were processed at the University of North

Dakota using the Airborne Data Processing and Analysis processing package (Delene, 2011). The

PDI data were processed at the University of Hawai'i. The 2D-S and HVPS-3 data were processed

160   using the University of Illinois/Oklahoma Optical Array Probe Processing Software (McFarquhar

et al., 2018). The data processing procedures followed to reject artifacts were summarized by

G21. Comparisons between the cloud probe data sets are described in the supplement.

The King hot-wire was used to sample LWC (hereafter King LWC). The PCASP was used to

sample the accumulation-mode aerosols sized from 0.1 to 3.0 μm. The PCASP $N(D)$ was used to

165   determine the out-of-cloud N_a. The CAS, CDP, PDI, 2D-S, and HVPS-3 collectively sampled the

number distribution function $N(D)$ for particles with diameter D from 0.5 to 19200 μm. The size

distribution covering the complete droplet size range was determined by merging the $N(D)$ for 3

< D < 50 μm with the $N(D)$ for 50 < D < 1050 μm from the *2D-S* and the $N(D)$ for 1050 < D < 19200

μm from the HVPS-3. The HVPS-3 sampled droplets with D > 1050 μm for a single 1 Hz data

170   sample across the PRFs analyzed in this study.

During each PRF, at least two independent measurements of $N(D)$ were made for 3 < D <

50 μm using the CAS, the PDI or a CDP (Table 1). The differences between the N_c and LWC derived

from the CAS, PDI and CDP $N(D)$ were quantified. The LWC estimates from the CAS, PDI, and CDP

were compared with the adiabatic LWC (LWC$_{ad}$) which represents the theoretical maximum for

175 LWC (Brenguier et al., 2000). The $N(D)$ for droplets with $D < 50$ μm was determined using the

probe which consistently had the LWC with better agreement with the LWC_{ad} during each IOP.

The differences between in-cloud data sets from different instruments were determined

using a two-sample t-test. The 95 % confidence intervals (CIs) between parameter means were

reported if the differences were statistically significant. During the 2017 IOP, the CAS and the

180 CDP-B sampled droplets with $D < 50$ μm. The CDP-B LWC was higher than the CAS LWC (95 % CIs:

0.11 to 0.12 g m^{-3} higher), and the average CDP-B LWC (0.18 g m^{-3}) had better agreement with

the average LWC_{ad} (0.24 g m^{-3}) compared to the average CAS LWC (0.08 g m^{-3}). Thus, the CDP-B

$N(D)$ was used to represent the $N(D)$ for droplets with $D < 50$ μm for the 2017 IOP.

Similar results were obtained when the CAS LWC and the CDP-B LWC were compared with

185 the LWC_{ad} for the 2018 IOP. During the 2018 IOP, the CDP-C was mounted at a different location

relative to the aircraft wing compared to the CAS and CDP-B, and the positions of CDP-B and CDP-

C were switched after 10 October 2018. O'Brien et al. (2021, in prep) found the CDP mounting

positions had only a 6 % impact on the calculation of N_c and the average CDP-B LWC and CDP-C

LWC were within 0.02 g m^{-3}. To maintain consistency with the 2017 IOP, data from the CDP

190 mounted next to the CAS were used for droplets with $D < 50$ μm for the 2018 IOP (except on 15

October 2018 when the CDP-C had a voltage issue).

During the 2016 IOP, measurements from the CDP-A were unusable for all PRFs due to an

optical misalignment issue. Nevertheless, the CAS and the PDI sampled droplets with $3 < D < 50$

μm. On average, the PDI LWC was higher than the CAS LWC (95 % CIs: 0.20 to 0.21 g m^{-3} higher).

195 Since the PDI LWC was greater than the LWC_{ad} (95 % CIs: 0.04 to 0.06 g m^{-3} higher), it was

hypothesized that the PDI LWC was an overestimate of the actual LWC. Thus, the *CAS N(D)* was used to represent the *N(D)* for droplets with *D* < 50 µm for the 2016 IOP.

The *2D-S* has two channels which concurrently sample the cloud volume. N_c and LWC were derived using data from the horizontal channel (N_H and LWC_H) and the vertical channel (N_V

200   and LWC_V). N_H and LWC_H were used for the 2016 IOP because N_V and LWC_V were not available due to soot deposition on the inside of the receive-side mirror of the vertical channel. N_H and N_V as well as LWC_H and LWC_V were strongly correlated for the 2017 and 2018 IOPs with Pearson's correlation coefficient $R \geq 0.92$ and the best-fit slope ≥ 0.90. The high correlation values suggest that little difference would have resulted from using the average of the two 2D-S channels. To

205   maintain consistency with the 2016 *IOP*, N_H and LWC_H were used for all three IOPs.

3 Cloud Properties

The *N(D)* from the merged droplet size distribution was integrated to calculate N_c. The 1 Hz data samples with $N_c > 10$ cm^{-3} and King *LWC* > 0.05 g m^{-3} were defined as in-cloud measurements (G21). In situ cloud sampling during ORACLES included flight legs when the P-3B

210   aircraft ascended or descended through the cloud layer (hereafter cloud profiles). Data from 329 cloud profiles with just under four hours of cloud sampling were examined (Table 1).

For every cloud profile, the cloud top height (Z_T) was defined as the highest altitude with $N_c > 10$ cm^{-3} and King LWC > 0.05 g m^{-3} (Table 2). The average Z_T during ORACLES was 1038 ± 270 m, where the uncertainty estimate refers to the standard deviation. Possner et al. (2020) found

215   that investigations of MSC in boundary layers shallower than 1 km can provide an underestimate of the LWP adjustments associated with ACIs. Z_T was used as a proxy for boundary layer height

and the average Z_T greater than 1 km suggests these measurements represent the complete range of LWP adjustments associated with ACIs.

The cloud base height (Z_B) was defined as the lowest altitude with $N_c > 10$ cm^{-3} and King

220 LWC > 0.05 g m^{-3}. In decoupled boundary layers, a layer of cumulus can be present below the stratocumulus layer with a gap between the cloud layers (Wood, 2012). Measurements from stratocumulus were used in this study and Z_B for the stratocumulus layer was identified as the altitude above which the King LWC increased without gaps greater than 25 m in the cloud sampling up to Z_T.

225 The difference between Z_T and Z_B was defined as H. Due to aerosol-induced changes in entrainment and boundary layer stability, the aerosol impact on H and Z_T can have the strongest influence on LWP adjustments associated with ACIs (Toll et al., 2019). Thus, the influence of ACIs on precipitation formation and S_o was examined as a function of H. Data collected during incomplete profiles of the stratocumulus or while sampling open-cell clouds (for example, on 2nd

230 October 2018) were excluded because of difficulties with estimating H for such profiles.

For each 1 Hz in-cloud data sample, the droplet size distribution was used to calculate R_e following Hansen and Travis (1974), where,

$$R_e = \int_3^\infty D^3 \, N(D) \, dD \bigg/ \int_3^\infty 2 \, D^2 \, N(D) \, dD \, . \tag{1}$$

LWC was calculated as

235 $$LWC \, (h) = \pi \, \rho_w / 6 \int_3^\infty D^3 \, N(D, h) \, dD \, , \tag{2}$$

where ρ_w is the density of liquid water and h is height in cloud above cloud base. LWC and King LWC were integrated over h from Z_B to Z_T to calculate LWP and King LWP, respectively. τ was calculated as

$$\beta_{ext}(h) = \int_3^\infty Q_{ext}\,\pi/4\,D^2\,N(D,h)\,dD\,,\quad \tau = \int_{Z_B}^{Z_T} \beta_{ext}(h)\,dh\,, \tag{3}$$

240   where β_{ext} is the cloud extinction and Q_{ext} is the extinction coefficient (approximately 2 for cloud droplets assuming geometric optics apply for visible wavelengths) (Hansen and Travis, 1974). The integrals in Eq. (1) to (3) were converted to discrete sums for $D > 3\ \mu m$ to consider the contributions of cloud drops, and not aerosols.

The total water mixing ratio (w_t) in a cloud is the sum of w_v and the liquid water mixing
245   ratio (w_l). At cloud base, $w_v = w_s$, where w_s is the saturation water vapor mixing ratio. w_l and w_s at Z_B were calculated as

$$w_l(Z_B) = LWC(Z_B)/\rho_a\,,\quad w_v(Z_B) = w_s = 1000\,\epsilon\,e_s(T, Z_B)/p(Z_B) - e_s(T, Z_B)\,, \tag{4}$$

where ρ_a is the density of air, ε is the ratio of the gas constants of air and water vapor, p is pressure, and e_s is the saturation water vapor pressure which depends on temperature (T). e_s
250   and w_s decrease with h because T decreases with h following the moist adiabatic lapse rate. For adiabatic clouds, w_t is constant and the adiabatic w_l increases with height as w_s decreases (the subscript 'ad' is added hereafter to denote adiabatic values). w_{lad} was multiplied by ρ_a to calculate LWC_{ad}. According to the adiabatic model (Brenguier et al., 2000), LWC_{ad} and LWP_{ad} are functions of H. These relationships help parameterize τ_{ad} as

255     $LWC_{ad}(h) = C_w\,h\,,\quad LWP_{ad} = 1/2\,C_w\,H^2\,,\quad \tau_{ad} \propto (\alpha\,C_w)^{-1/6}\,(kN_c)^{1/3}\,LWP^{5/6}\,,$ (5)

where C_w is condensation rate, α is cloud adiabaticity (LWP divided by LWP$_{ad}$), and k is

droplet spectrum width (Brenguier et al., 2000). C_w is a function of the cloud base p and T

(Brenguier et al., 2000) and α helps quantify the impact of entrainment mixing or precipitation

on cloud water. Assuming constant C_w (1.44 to 2) or α (0.6 to 1) can lead to errors in satellite

260   retrievals of N_c (Janssen et al., 2011; Merk et al., 2016; Grosvenor et al., 2018) which motivates

the need for in situ estimates of C_w and α. C_w was calculated using a regression model to fit LWP$_{ad}$

as a function of H. LWP$_{ad}$ was a quadratic function of H (Figure 2) with $R \geq 0.93$. The average C_w

for the three IOPs was 2.71 ± 0.30 g m^{-3} km^{-1} (Table 3). This was greater than C_w for MSC over the

northeast Pacific (2.33 g m^{-3} km^{-1}) (Braun et al., 2018).

265   For 304 cloud profiles with LWP$_{ad}$ > 5 g m^{-2}, the average α was 0.72 ± 0.31 (0.85 ± 0.41 if

the King hot-wire was used to represent LWC). This was consistent with α for MSC over the

northeast Pacific (0.77 ± 0.13) (Braun et al., 2018) and the southeast Pacific (median α = 0.7 to

0.8) (Min et al., 2012). The differences between LWP$_{ad}$ and LWP increased with H. For example,

when the profiles were divided into thin (H < 175 m) and thick clouds (H > 175 m) based on the

270   median H, thin clouds had higher α (0.84 ± 0.34) than thick clouds (0.60 ± 0.23). The inverse

relationship between α and H is consistent with previous MSC observations (Braun et al., 2018).

4 Aerosol Influence on Cloud Microphysics

The MSC over the southeast Atlantic were overlaid by biomass-burning aerosols from

southern Africa (Adebiyi and Zuidema, 2016; Redemann et al., 2021) with instances of contact

275   and separation between the MSC cloud tops and the base of the biomass burning aerosol layer

(G21). Across the three IOPs, 173 profiles were conducted at locations where an extensive

Atmospheric
Chemistry
and Physics
Discussions

Open Access

EGU

aerosol plume with $N_a > 500$ cm^{-3} was located within 100 m above Z_T (hereafter, contact profiles) (Table 1). 156 profiles were conducted at locations where the level of $N_a > 500$ cm^{-3} was located at least 100 m above Z_T (hereafter, separated profiles). About 50 % of the in situ cloud sampling across the three IOPs was conducted during contact profiles (Table 1). Due to inter-annual variability, contact profiles accounted for about 42 %, 91 %, and 39 % of the in situ cloud sampling during the 2016, 2017, and 2018 IOPs, respectively.

The average N_c and R_e for all cloud profiles across the three IOPs were 157 ± 96 cm^{-3} and 8.2 ± 2.7 µm, respectively (Table 3). The high proportion of contact profiles during the 2017 IOP was associated with higher average N_c and lower average R_e (229 cm^{-3} and 6.9 µm) compared to the 2016 IOP (150 cm^{-3} and 7.0 µm) and the 2018 IOP (132 cm^{-3} and 9.8 µm). It is possible that the use of CDP-B data for the 2017 IOP contributed to the increase in average N_c relative to the 2016 IOP. However, the difference between the average CAS N_c and the average CDP-B N_c for the 2017 IOP (12 cm^{-3}) was lower than the difference between the average N_c for the 2016 and 2017 IOPs (79 cm^{-3}). The difference between the N_c for these IOPs were thus primarily due to the conditions at the cloud sampling locations. The microphysical differences between the 2016 and 2017 IOPs were associated with differences in surface precipitation. Based on the W-band retrievals from the Jet Propulsion Laboratory Airborne Precipitation Radar Version 3, the 2017 IOP had fewer profiles with precipitation reaching the surface (13 %) compared to the 2016 IOP (34 %) (Dzambo et al., 2019).

On average, contact profiles had significantly higher N_c (95 % CIs: 84 to 90 cm^{-3} higher) and lower R_e (95 % CIs: 1.4 to 1.6 µm lower) compared to separated profiles (throughout the

Atmospheric
Chemistry
and Physics
Discussions

Open Access

EGU

study, the term "significant" is exclusively used to represent statistical significance). The significant differences in N_c and R_e were associated with significantly higher τ (95 % CIs: 0.04 to

300   3.06 higher) for contact profiles, in accordance with the Twomey effect (Twomey, 1974; 1977). These results were consistent with the 2016 IOP when the contact profiles had higher N_c (95 % CIs: 60 to 68 cm^{-3} higher), lower R_e (95 % CIs: 1.1 to 1.3 μm lower), and higher τ (95 % CIs: 1.1 to 4.3 higher) (G21).

The median N_c increased as a function of normalized height above cloud base (Z_N) for Z_N

305   ≤ 0.25 consistent with droplet nucleation (Figure 3a). The median N_c decreased near cloud top for Z_N ≥ 0.75 from 204 to 154 cm^{-3} for contact and from 104 to 69 cm^{-3} for separated profiles. This was consistent with droplet evaporation associated with cloud-top entrainment (G21). The median R_e increased with Z_N consistent with condensational growth (Figure 3b). There was a greater increase in the median R_e from cloud base to cloud top for separated profiles (from 7.1

310   to 9.5 μm) compared to contact profiles (from 6.1 to 7.9 μm). This is consistent with previous observations of stronger droplet growth in cleaner conditions as a function of Z_N (Braun et al., 2018; G21) and LWP (Rao et al., 2020). Statistically insignificant differences between the average H for contact and separated profiles suggest that the differential droplet growth was associated differences in cloud processes like collision-coalescence (further discussed in Section 5).

315   Eq. (5) shows the relative dependence of τ_{ad} on N_c and LWP. The LWC and LWP responses to changes in aerosol conditions were examined because the adiabatic model suggests $\tau \propto$ LWP$^{5/6}$ (Eq. 5) (Brenguier et al., 2000). Contact profiles had significantly higher LWC, but the relative increase was less than 10 % (Table 4). It is possible this represents the lower limit of the aerosol

influence on cloud water since the aerosol influence varies with droplet size, precipitation

320   formation processes (Section 5), and the buffering by meteorological conditions (Section 7).

LWC was divided into rainwater content (RWC) and cloud water content (CWC) based on droplet size. Droplets with $D > 50$ μm were defined as drizzle (Abel and Boutle, 2012; Boutle et al., 2014) and the total drizzle mass was defined as RWC. The droplet mass for $D < 50$ μm was defined as CWC. RWP and CWP were defined as the vertical integrals of RWC and CWC,

325   respectively. The median CWC increased with Z_N but decreased over the top 10 % of the cloud layer for contact profiles and over the top 20 % of the cloud layer for separated profiles consistent with cloud-top entrainment (Figure 3c). For contact profiles, the median RWC increased with Z_N before decreasing for $Z_N \geq 0.75$. The median RWC for separated profiles varied with Z_N. The bottom half of the cloud layer had higher median values (up to 8.7 x 10^{-3} g m^{-3}) compared to the

330   top half (up to 7.0 x 10^{-3} g m^{-3}) (Figure 3d).

For contact profiles, there was a significant increase in the average CWC (10 %) and a significant decrease in the average RWC (60 %) compared to separated profiles (Table 4). Contact profiles also had significantly lower average RWP with insignificant differences for average CWP (Table 4). Contact profiles were located in deeper boundary layers with significantly higher Z_B and

335   Z_T compared to separated profiles. However, the decrease in RWC cannot be attributed to differences in H or LWP (Kubar et al., 2009) because of statistically similar H and LWP for contact and separated profiles, on average (Table 4). These results show that instances of contact between above-cloud aerosols and the MSC were associated with more numerous and smaller

cloud droplets and weaker droplet growth compared to instances of separation between the

340 above-cloud aerosols and the MSC.

5 Precipitation Formation and H

Precipitation rate R_p was calculated using the drizzle water content and fall velocity $u(D)$ following Abel and Boutle (2012),

$$R_p = \pi/6 \int_{50\ \mu m}^{\infty} n(D)D^3 u(D)dD \qquad (6)$$

345 with fall velocity relationships from Rogers and Yau (1989) used in the computation.

Contact profiles had significantly lower R_p compared to separated profiles (95 % CIs: 0.03 to 0.05 mm h^{-1} lower). This suggests contact between the MSC and above-cloud biomass burning aerosols was associated with precipitation suppression. LWP and H impact the sign and magnitude of the precipitation changes in response to changes in aerosol conditions (Kubar et

350 al., 2009; Christensen and Stephens, 2012). Thus, cloud and precipitation properties were evaluated as a function of H to examine the aerosol-induced changes in precipitation formation.

The 95th percentile was used to represent the maximum value of a variable. For example, the 95th percentile of R_p (denoted by R_{p95}) represents the maximum R_p during a cloud profile. Although more numerous contact profiles were drizzling compared to separated profiles, the

355 latter had more numerous profiles with high precipitation intensity. For instance, 114 out of 173 contact and 95 out of 156 separated profiles were drizzling with $R_{p95} > 0.01$ mm h^{-1}, out of which 36 contact and 40 separated profiles had $R_{p95} > 0.1$ mm h^{-1}, and only 1 contact and 9 separated

profiles had R_{p95} > 1 mm h⁻¹ (Figure 4a). This is consistent with radar retrievals of surface R_p < 1 mm h⁻¹ for over 93 % of the radar profiles from 2016 and 2017 (Dzambo et al., 2019).

5.1. Microphysical properties

On average, separated profiles had greater R_{p95} (0.22 mm h⁻¹) compared to contact profiles (0.07 mm h⁻¹). R_{p95} was positively correlated with H as thicker profiles had higher precipitation intensity (Figure 4a). The average R_{p95} increased from thin (H < 175 m) to thick clouds (H > 175 m) from 0.04 to 0.10 mm h⁻¹ for contact and 0.13 to 0.29 mm h⁻¹ for separated profiles. Precipitation intensity thus decreased from separated to contact profiles for both thin and thick profiles. The average R_{p95} for thin and thick contact profiles were 32 % and 37 % of the average R_{p95} for thin and thick separated profiles, respectively.

CWC$_{95}$ was positively correlated with H as thicker clouds had higher droplet mass (Figure 4b). This was consistent with condensational and collision-coalescence growth continuing to occur with greater height above cloud base (Figure 3b, c), and greater cloud depth allowing for greater droplet growth. N_{c95} and R_{e95} were negatively and positively correlated with H, respectively (Figure 4c, d). The trends in N_c and R_e versus H were consistent with the process of collision-coalescence resulting in fewer and larger droplets.

On average, contact profiles had higher N_{c95} and lower R_{e95} (311 cm⁻³ and 8.6 µm) compared to separated profiles (166 cm⁻³ and 10.8 µm). It can be inferred that the presence of more numerous and smaller droplets during contact profiles decreased the efficiency of collision-coalescence. Alternatively, there may not have been sufficient time during the ascent to produce the few large droplets needed to broaden the size distribution and initiate collision-coalescence.

Atmospheric
Chemistry
and Physics
Discussions

Open Access

EGU

Since contact and separated profiles had statistically similar H (Table 4), the following discussion

380   examines the link between precipitation suppression and the aerosol-induced changes in N_c, R_e,

and LWC and their impact on precipitation.

5.2. Precipitation properties

Precipitation formation process rates were estimated using equations used in numerical

models to compare precipitation formation between contact and separated profiles.

385   Precipitation development in models is explained using bulk microphysical schemes. GCMs or LES

models parameterize precipitation formation using S_{AUTO} and S_{ACC} (e.g., Penner et al., 2006;

Morrison and Gettelman, 2008; Gordon et al., 2018). The most commonly used

parameterizations were used to estimate equivalent rates of precipitation formation from

models. S_{AUTO} and S_{ACC} were calculated following Khairoutdinov and Kogan (2000),

390
$$S_{AUTO} = (dw_r)_{AUTO} \, /dt = 1350 \, w_c^{2.47} N_c^{-1.79} \tag{7}$$

and

$$S_{ACC} = (dw_r)_{ACC}/dt \; = 67 \, (w_c w_r)^{1.15} \tag{8}$$

where w_c and w_r are cloud water and rainwater mixing ratios, respectively, and equal to the CWC

and RWC divided by ρ_a.

395   Contact profiles had significantly lower S_{AUTO} and S_{ACC} compared to separated profiles (Table 4).

This is consistent with significantly lower RWC and R_p for contact profiles and the association of

S_{AUTO} and S_{ACC} with precipitation onset and precipitation intensity, respectively. S_{AUTO95} and S_{ACC95}

were positively correlated with H (Figure 5a, b). Separated profiles had higher S_{AUTO95} and S_{ACC95}

(9.6 x 10^{-10} s^{-1} and 2.2 x 10^{-8} s^{-1}) compared to contact profiles (2.9 x 10^{-10} s^{-1} and 1.2 x 10^{-8} s^{-1})

400   associated with the inverse relationship between S_{AUTO} and N_c (Eq. 7). Faster autoconversion

resulted in higher drizzle water content and greater accretion of droplets on drizzle drops.

The sampling of lower N_{c95} and higher R_{e95} compared to thinner profiles suggests that

collision-coalescence was more effective in profiles with higher H (Figure 4c, d). Thin contact

profiles had the lowest S_{AUTO95} (1.4 x 10^{-10} s^{-1}) followed by thick contact (4.5 x 10^{-10} s^{-1}), thin

405   separated (4.7 x 10^{-10} s^{-1}), and thick separated profiles (1.4 x 10^{-9} s^{-1}). High N_c and low CWC for

thin contact profiles (Figure 4b, c) are consistent with increased competition for cloud water

leading to weaker autoconversion. It is hypothesized that these microphysical differences

resulted in the lower S_{AUTO95} and R_{p95} for thin contact profiles compared to other profiles. The

differences between R_p for contact and separated profiles thus varied with H in addition to N_c,

410   R_e, and CWC. N_c, R_e, and CWC varied with N_a (Section 4) and ACIs were examined in Sections 6

and 7.

6 Aerosol Influence on Precipitation

6.1. Below-cloud N_a

Polluted boundary layers in the southeast Atlantic are associated with entrainment

415   mixing between the free troposphere and the boundary layer (Diamond et al., 2018). For the

2016 IOP, contact profiles were located in boundary layers with significantly higher N_a (95 % *CIs*:

93 to 115 cm^{-3} higher) and carbon monoxide (CO) (95 % *CIs*: 13 to 16 ppb higher) compared to

separated profiles (G21). This is consistent with data from all three IOPs when contact profiles

were located in boundary layers with higher N_a (95 % CIs: 231 to 249 cm^{-3} higher) and CO (95 %

420   CIs: 27 to 29 ppb higher).

Following G21, 171 contact and 148 separated profiles from the IOPs were classified into

four regimes, Contact, high N_a (C-H), Contact, low N_a (C-L), Separated, high N_a (S-H), and

Separated, low N_a (S-L), where "low N_a" meant the profile was in a boundary layer with $N_a < 350$

cm^{-3} up to 100 m below cloud base. Boundary layer CO concentration above 100 ppb was

425   sampled during 107 contact and 31 separated profiles, respectively. Contact profiles were more

often located in high N_a boundary layers (131 out of 171 profiles classified as C-H) while separated

profiles were more often located in low N_a boundary layers (108 out of 148 profiles classified as

S-L). This suggests contact between MSC cloud tops and above-cloud biomass burning aerosols

was associated with the entrainment of biomass-burning aerosols into the boundary layer.

430   Contact profiles had significantly higher N_c and significantly lower R_e relative to separated

profiles in both high N_a (C-H relative to S-H) and low N_a (C-L relative to S-L) boundary layers

(Figure 6). This was associated with significantly higher above- and below-cloud N_a for the contact

profiles (Table 5). The differences in N_c and R_e were higher in high N_a boundary layers where the

differences in above- and below-cloud N_a were also higher compared to low N_a boundary layers

435   (Table 5). This was consistent with previous observations of MSC cloud properties (Diamond et

al., 2018; Mardi et al., 2019) and similar analysis for data from the 2016 IOP (G21).

C-L profiles had significantly higher N_c (95 % CIs: 5 to 14 cm^{-3} higher) compared to S-H

profiles despite having significantly lower below-cloud N_a (95 % CIs: 69 to 85 cm^{-3} lower).

Significantly higher above-cloud N_a for C-L profiles (95 % CIs: 321 to 361 cm^{-3} higher) suggests

440 that this was associated with the influence of above-cloud N_a on N_c. However, the smaller difference in N_c compared to the differences between C-H and S-H or C-L and S-L profiles suggests the combined impact of above- and below-cloud N_a was stronger than the impact of above-cloud N_a alone. These comparisons were qualitatively consistent when thresholds of 300 cm^{-3} or 400 cm^{-3} were used to define a low N_a boundary layer.

445 **6.2. N_c and R_p versus H**

The cloud profiles were divided into four populations based on H to compare N_c and R_p between different aerosols conditions while H was constrained. The populations were defined using the quartiles of H (129, 175, and 256 m) to ensure similar sample sizes (Table 6). For each population, contact profiles had higher N_c and lower R_p (Figure 7a, b) consistent with comparisons

450 averaged over all profiles (Table 4). The average N_c decreased and the average R_p increased with H (Figure 7a, b). For contact profiles, the average N_c decreased with H from 221 to 191 cm^{-3} and the average R_p increased from 0.03 to 0.07 mm h^{-1}. For separated profiles, the average N_c decreased from 149 to 92 cm^{-3} and the average R_p increased from 0.06 to 0.21 mm h^{-1} over the same range of H. These trends show the impact of collision-coalescence with increasing H.

455 For C-H profiles, high above- and below-cloud N_a were associated with the highest average N_c and the lowest average R_p among the four regimes (Figure 7c, d). C-H profiles had the smallest increase in the average R_p with H (0.02 to 0.04 mm h^{-1}). Conversely, for S-L profiles, low above- and below-cloud N_a were associated with the lowest average N_c, the highest average R_p, and the highest increase in the average R_p with H (0.12 to 0.29 mm h^{-1}). For each regime, the

460 average N_c decreased with H (except C-L) and the average R_p increased with H (Figure 7c, d).

6.3. Precipitation Susceptibility S_o

S_o was used to evaluate the dependence of R_p on N_c under the different aerosol conditions. S_o, defined as the negative slope between the natural logarithms of R_p and N_c (Feingold and Seibert, 2009), is given by

465 $$S_o = -\, d \ln(R_p)/d \ln(N_c)\,, \tag{9}$$

where a positive value indicates decreasing R_p with increasing N_c, in accordance with the "lifetime effect" (Albrecht, 1989). The average S_o across all profiles was 0.88 ± 0.03. On average, contact profiles had lower S_o (0.87 ± 0.04) compared to separated profiles (1.08 ± 0.04). This was consistent with the hypothesis of lower values for S_o analogues (where N_c in Eq. (9) is replaced

470 by N_a) in the presence of above-cloud aerosols (Duong et al., 2011). Modelling studies (Wood et al., 2009; Jiang et al., 2010) have found S_o depends on the ratio of S_{ACC} to S_{AUTO}. S_{ACC} is independent of N_c (Eq. 8) and greater values of S_{ACC}/S_{AUTO} represent a weaker dependence of R_p on N_c. Lower S_o for contact profiles was associated with higher S_{ACC}/S_{AUTO} compared to separated profiles (Table 4).

475 S_o was calculated as a function of H (Figure 8) using N_c and R_p for the four populations of cloud profiles (Figure 9). The sensitivity of S_o to the number of populations is discussed in Appendix A. Averaged over all profiles, S_o had minor variations with H (e.g., 0.67, 0.68, and 0.54 as H increased) before increasing to 1.13 for $H > 256$ m (Table 6). This trend in S_o versus H was consistent with previous analyses of S_o (Sorooshian et al., 2009; Jung et al., 2016). However,

480 different trends emerged when S_o was calculated for contact and separated profiles.

The difference between S_o for contact and separated profiles varied with H and thin clouds ($H < 129$ m) had the highest difference. 30 separated profiles with $H < 129$ m had high S_o (1.47 ± 0.10). This was because of strong dependence of R_p on N_c associated with higher average R_p for low N_c (< 100 cm^{-3}) measurements (0.18 mm h^{-1}) compared to high N_c measurements (0.01

485   mm h^{-1}) (Figure 9a). In contrast, precipitation suppression and weaker droplet growth for thin contact profiles (Section 5) resulted in average $R_p < 0.03$ mm h^{-1} for both low N_c and high N_c measurements (Fig. 9a). Thus, there was poor (and statistically insignificant) correlation between N_c and R_p ($R = -0.03$) which led to a low and statistically insignificant value for S_o (-0.06 ± 0.11).

For separated profiles, S_o decreased with H to 0.53 ± 0.09 for $129 < H < 175$ m and to 0.34

490   ± 0.07 for $175 < H < 256$ m (Figure 8a). This was because the average R_p for the high N_c measurements increased with H from 0.01 mm h^{-1} for thin profiles to 0.05 and 0.04 mm h^{-1}, respectively (Figure 9b, c). This was consistent with collision-coalescence beginning to occur for high N_c measurements as droplet mass increased with H (Figure 5b). S_o increased to 1.45 ± 0.07 for the cloud population with $H > 256$ m. This population had lower N_c and higher R_p compared

495   to the populations with lower H (Figure 7a, b). The average R_p for low N_c measurements (0.26 mm h^{-1}) was higher than high N_c measurements (0.13 mm h^{-1}) (Figure 9d). These observations were consistent with collision-coalescence and stronger precipitation formation for low N_c measurements. The latter was associated with the inverse relationship between N_c and S_{AUTO}.

Contact profiles with $H > 129$ m had a significant correlation between N_c and R_p. The

500   average R_p increased with H with a larger increase for the low N_c measurements (0.028 to 0.12 mm h^{-1}) compared to the high N_c measurements (0.03 to 0.06 mm h^{-1}). It is hypothesized that

collision-coalescence was hindered by the presence of more numerous droplets during the high N_c measurements, and as droplet growth and collision-coalescence occurred with increasing H, the limiting factor for R_p changed from H to N_c. The dependence of R_p on N_c increased with H and

505   as a result, S_o increased with H from 0.88 ± 0.06 to 1.15 ± 0.06 (Figure 8a).

S-L profiles had the highest S_o (1.12) among the four regimes defined based on the above- and below-cloud N_a (Table 7). This was associated with the S-L profiles having the lowest average N_c and the highest average R_p among the four regimes (Figure 7c, d). In descending order of S_o, S-L profiles were followed by C-L (0.86), S-H (0.50), and C-H profiles (0.33). Profiles in low N_a

510   boundary layers (S-L and C-L) had higher S_o compared to profiles in high N_a boundary layers (S-H and C-H). This was consistent with wet scavenging of below-cloud aerosols (Duong et al., 2011; Jung et al., 2016).

The sensitivity of S_o to the inclusion of precipitating clouds is examined in Appendix B. C-L and C-H profiles had similar trends in S_o except for the thinnest profiles (H < 129 m) (Figure 8b).

515   C-L profiles had an insignificant value for S_o due to low sample size (4) and C-H profiles had negative S_o. These were thin profiles with little cloud water (Figure 5b), high N_c (Figure 7c), and low R_p (Figure 7d). It is hypothesized that increasing N_c would provide the cloud water required for precipitation initiation and aid collision-coalescence.

107 out of 148 separated profiles were classified as S-L profiles. As a result, separated and

520   S-L profiles had similar trends in S_o versus H (Figure 8). On average, S-L profiles had higher S_o than S-H profiles which could be associated with wet scavenging resulting in the lower below-cloud N_a for S-L profiles. For S-H profiles, S_o was constant with H at about 0.45 (except for the population

with 175 < H < 256 m which had an insignificant value for S_o) (Table 7). The S_o comparisons

between profiles located in high N_a or low N_a boundary layers varied with the sample sizes of the

525 populations. The sample sizes varied based on the threshold used to define a low N_a boundary

layer which is discussed in Appendix C.

6.4. S_o Discussion

Higher N_c and lower R_e for contact profiles led to precipitation suppression and lower

S_{AUTO}, S_{ACC}, and R_p which were associated with lower S_o compared to separated profiles. Polluted

530 clouds were thus less susceptible to precipitation suppression than cleaner clouds. The

differences in S_o varied with H due to the variability in R_p, N_c, R_e, and CWC associated with aerosols

and droplet growth. The change in S_o was highest for thin polluted clouds due to poor correlation

between N_c and R_p as limited droplet growth led to low R_p regardless of the N_c. Power-law

relationships between R_p, N_c, and H (Geoffroy et al., 2008) thus need to account for changes in

535 the dependence of R_p on N_c/H associated with ACIs and H.

The trends in S_o were only compared with studies analyzing airborne data due to the

variability in S_o depending on whether aircraft, remote sensing, or modeling data were examined

(Sorooshian et al., 2019). Consistent with Terai et al. (2012), S_o decreased with H for separated

profiles with H < 256 m. The results from Section 5 suggest droplet growth with H decreased the

540 susceptibility to aerosols because R_p was limited by droplet growth instead of N_a or N_c. In

comparison, S_o increased with H for contact profiles consistent with Jung et al. (2016). The low S_o

for thin contact profiles was consistent with the low S_o (0.06) for thin MSC over the southeast

Pacific (Jung et al., 2016). This was attributed to insufficient cloud water for precipitation initiation (as noted in Section 5).

545   Jung et al. (2016) analyzed MSC sampled farther east and away from South America compared to Terai et al. (2012). They argued a westward increase in precipitation frequency and intensity, along with a decrease in aerosols and N_c, led to the differences between the two studies. This same attribution on the role of aerosols can be made for the ORACLES data as there were differences between contact and separated profiles because the MSC sampled during these

550   profiles were located in similar geographical locations with different aerosol conditions. Modeling studies (e.g., Wood et al., 2009; Gettelman et al., 2013) have shown that S_o increases with H when S_{AUTO} dominates S_{ACC} (typically for $R_e < 14$ μm, the critical radius for precipitation initiation). Maximum $R_e < 14$ μm was sampled during all but 23 separated and 3 contact profiles (Figure 5d). This would explain the increase in S_o with H for both contact (for $H > 129$ m) and

555   separated profiles (for $H > 256$ m).

7 Meteorological Influence on LWP

The relationships between LWP or H and N_c, R_e, and LWC depend on meteorological conditions in addition to aerosol properties. The MSC LWP and cloud cover can vary with LTS (Klein and Hartmann, 1993; Mauger and Norris, 2007), estimated inversion strength (EIS) (Wood

560   and Bretherton, 2006), and SST (Wilcox, 2010; Sakaeda et al., 2011). The correlations between LWP/H and these parameters are examined using the European Centre for Medium-Range Weather Forecasts (ECMWF) atmospheric reanalysis (ERA5) (Hersbach et al., 2020) to define the meteorological conditions.

ERA5 provides hourly output with a horizontal resolution of 0.25° x 0.25° for 37 pressure

565   (p) levels (up to 1 hPa). The cloud sampling for most flights was conducted within three hours of

12:00 UTC (Table 2). ERA5 data at 12:00 UTC were thus used for the grid box nearest to the profile

(Dzambo et al., 2019). The low cloud cover (LCC), SST, H_{BL}, total column liquid water (ERA5 LWP)

and rainwater (ERA5 RWP), mean sea level pressure (p_o), 2 m temperature (T_o), and 2 m dew

point temperature (T_d) were examined (Table 8).

570   The difference between potential temperatures at 700 hPa and the surface was defined

as LTS (Klein and Hartmann, 1993). The lifting condensation level (LCL) was defined as LCL = 125

m K^{-1} (T_o - T_d) (Lawrence, 2005). EIS was calculated following Wood and Bretherton (2006),

$$EIS = LTS - \Gamma_m^{850}(z_{700} - LCL), \ \Gamma_m^{850} = \Gamma_m([T_o + T_{700}]/2 , 850 \, mb) , \qquad (10)$$

where Γ_m is the moist adiabatic potential temperature gradient and z_{700} is the height at 700 mb.

575   Γ_m was calculated as

$$\Gamma_m(T,p) = \frac{g}{c_p}\left[1 - \frac{1 + L_v w_s(T,p)/R_a T}{1 + L_v^2 w_s(T,p)/c_p R_v T^2}\right], \qquad (11)$$

where g is the gravitational acceleration, c_p is the specific heat of air at constant pressure, L_v is

the latent heat of vaporization, and R_a and R_v are the gas constants for dry air and water vapor,

respectively (Wood and Bretherton, 2006).

580   LCC refers to cloud fraction for $p > 0.8 \, p_o$, corresponding to $p > 810$ hPa, where most

profiles were sampled (Table 2). The ECMWF model used a threshold of EIS > 7 K to distinguish

between well-mixed boundary layers topped by stratocumulus and decoupled boundary layers

Atmospheric
Chemistry
and Physics
Discussions
Open Access
EGU

with cumulus clouds (ECMWF IFS Documentation, 2016). This distinction improved the agreement between the model LCC and LWP and observations (Köhler et al., 2011).

585   LCC was proportional to EIS/LTS, and LCC < 0.8 was mostly observed for EIS < 7 K (Figure 10a). Decoupled boundary layers can be topped by MSC (G21; Wood, 2012). Profiles with EIS < 7 K were included in the analysis if ERA5 had LCC > 0.95. This included 64 contact and 88 separated profiles from the three IOPs. For the 2016, 2017, and 2018 IOPs, 50, 20, and 76 profiles, respectively, had LCC > 0.95 out of which, 0, 4, and 44 profiles, respectively, had EIS < 7 K. The

590   average ERA5 H_{BL} (599 ± 144 m) was lower than the average Z_T (932 ± 196 m). This underestimation of H_{BL} by ERA5 has been observed for stratocumulus over the southeast and northeast Pacific (Ahlgrimm et al., 2009; Hannay et al., 2009).

On average, the ERA5 LWP (51 ± 21 g m^{-2}) was slightly greater than LWP (46 ± 41 g m^{-2}), but the differences were statistically insignificant. There was a significant but weak correlation

595   between LWP and ERA5 LWP (R = 0.18) (Figure 10b). On average, the ERA5 RWP (0.48 ± 1.07 g m^{-2}) was lower than RWP (1.19 ± 2.76 g m^{-2}). There were insignificant differences between ERA5 LWP/LWP for contact and separated profiles with LCC > 0.95 (Table 8). Contact profiles with LCC > 0.95 had significantly higher ERA5 RWP (Table 8). While this is counter-intuitive, given the precipitation suppression, it was due to selection of profiles with LCC > 0.95. Contact profiles with

600   LCC > 0.95 also had higher in situ RWP (95 % CIs: 0.32 to 2.08 g m^{-2} higher) compared to separated profiles with LCC > 0.95.

LWP was positively correlated with SST and T_o and negatively correlated with LTS and EIS with weak but statistically significant correlations (Figure 11). On average, separated profiles had

605   significantly higher SST (95 % CIs: 0.01 to 1.48 K higher) compared to contact profiles with
insignificant differences between the average T_o, EIS, and LTS. Since the correlation between
LWP/H and SST was weak, it is unlikely the differences between contact and separated profiles
were driven by SST differences alone. When all profiles (irrespective of LCC) were considered,
there were insignificant differences between the average ERA5 RWP, SST, T_o, EIS, and LTS for
contact and separated profiles. This suggests the differences between contact and separated

610   profiles found during the ORACLES IOPs were primarily associated with ACIs instead of
meteorological effects.

8 Conclusions

In situ measurements of stratocumulus over the southeast Atlantic Ocean were collected
during the NASA ORACLES field campaign. The microphysical (N_c and R_e), macrophysical (LWP and

615   H), and precipitation properties (R_p and S_o) of the stratocumulus were analyzed. 173 "contact"
profiles with $N_a > 500$ cm^{-3} within 100 m above cloud tops were compared with 156 "separated"
profiles with $N_a < 500$ cm^{-3} up to at least 100 m above cloud tops. Contact between above-cloud
aerosols and the stratocumulus was associated with,

1. More numerous and smaller droplets with weaker droplet growth with height.

620   Contact profiles had significantly higher N_c (84 to 90 cm^{-3} higher) and lower R_e (1.4 to 1.6
µm lower) compared to separated profiles. The median R_e had a smaller increase from cloud base
to cloud top for contact (6.1 to 7.9 µm) compared to separated profiles (7.1 to 9.5 µm). The
profiles had similar LWP and H, and it is hypothesized the differences in droplet growth were
associated with collision-coalescence.

625   2. The entrainment of above-cloud biomass-burning aerosols into the boundary layer and aerosol-induced cloud microphysical changes in both clean and polluted boundary layers.

Contact profiles were more often located in polluted boundary layers and had higher below-cloud CO concentration (27 to 29 ppb higher). Contact profiles had 25 to 31. cm^{-3} higher N_c and 0.2 to 0.5 µm lower R_e in clean and 98 to 108 cm^{-3} higher N_c and 1.6 to 1.8 µm lower R_e in

630   polluted boundary layers.

3. Precipitation suppression with significantly lower precipitation intensity and precipitation formation process rates.

Separated profiles had R_p up to 0.22 mm h^{-1} while contact profiles had R_p up to 0.07 mm h^{-1}. S_{AUTO} and S_{ACC} had higher maxima for separated (up to 9.6 x 10^{-10} s^{-1} and 2.2 x 10^{-8} s^{-1})

635   compared to contact profiles (up to 2.9 x 10^{-10} s^{-1} and 1.2 x 10^{-8} s^{-1}).

4. Lower precipitation susceptibility with the strongest impact in thin clouds (H < 129 m).

Contact profiles had lower S_o (0.87 ± 0.04) compared to separated profiles (1.08 ± 0.04). Thin clouds had the highest difference in S_o (-0.06 ± 0.11 for contact and 1.47 ± 0.10 for separated). Lower S_o for thin contact profiles was associated with poor correlation between N_c

640   and R_p (R = -0.03). For separated profiles, S_o decreased with H before increasing for H > 256 m. In comparison, S_o increased with H for contact profiles for H > 129 m.

5. Statistically insignificant differences in meteorological parameters that influence LWP/H.

Based on ERA5 reanalysis data, LWP was correlated with SST (R = 0.22), T_o (R = 0.27), LTS (R = - 0.29), and EIS (R = - 0.31). Contact profiles with ERA5 LCC > 0.95 had lower SST (0.01 to 1.48

645   K lower) with similar T_o, LTS, and EIS compared to separated profiles. The SST differences were insignificant when profiles with LCC < 0.95 were included in the comparison.

     The ORACLES dataset addresses the "lack of long-term data sets needed to provide statistical significance for a sufficiently large range of aerosol variability influencing specific cloud regimes over a range of macrophysical conditions" (Sorooshian et al., 2010). Three important

650   factors affecting S_o were discussed (Sorooshian et al., 2019): above-cloud N_a, below-cloud N_a, and meteorological conditions. This study analyzed ORACLES data from all three IOPs and the first two conclusions were consistent with the analysis of ORACLES 2016 (Gupta et al., 2021). Future work will compare in situ data with R_p retrievals from the Airborne Precipitation Radar (Dzambo et al., 2021) to evaluate the sensitivity of S_o to the use of satellite retrievals of R_p (Bai et al., 2018).

655   Vertical profiles of MSC cloud properties will be used to evaluate satellite retrievals (Painemal and Zuidema, 2011; Zhang and Platnick, 2011) to address the uncertainties associated with satellite-based estimates of ACIs (Quaas et al., 2020).

660

APPENDIX A – Sensitivity studies on dependence of S_o on H

665   The base analysis examined how cloud properties varied with H by separating cloud profiles into four populations of H using the following endpoints: 28, 129, 175, 256, and 700 m. Two sensitivity studies determine if trends describing the variation of N_c, R_p, and S_o with H were sensitive to the endpoints used to sort cloud profiles into different populations.

     First, cloud profiles were classified into two populations using the median H (175 m) to
670 divide the populations (Table A1). The average N_c decreased and the average R_p increased with H for both contact (211 to 186 cm^{-3} and 0.03 to 0.07 mm h^{-1}) and separated profiles (129 to 104 cm^{-3} and 0.07 to 0.15 mm h^{-1}). S_o increased with H for contact profiles from 0.53 to 1.06 and slightly decreased with H for separated profiles from 1.05 to 1.02 (Table A1). The difference between S_o for contact and separated profiles was greater for thin profiles ($H < 175$ m) compared
675 to thick profiles ($H > 175$ m). These results are consistent with trends using four populations but provide less detail about how S_o varies with H (Fig. A1).

     Second, cloud profiles were classified into three populations using the terciles of H (145 and 224 m) (Table A1). The average N_c decreased and the average R_p increased from the lowest to the highest H for contact (231 to 187 cm^{-3} and 0.03 to 0.07 mm h^{-1}) and separated profiles (138
680 to 95 cm^{-3} and 0.06 to 0.18 mm h^{-1}). For separated profiles, S_o first decreased with H from 1.15 to 0.25 before increasing to 1.45 for the highest H (Fig. A1). Contact profiles had insignificant S_o for the lowest H followed by S_o increasing from 0.95 to 1.08 with H. The results presented here are robust as relates to the number of populations used.

685 **APPENDIX B – Sensitivity studies on dependence of S_o on R_p**

Another sensitivity study examined the R_p threshold used for cloud profiles included while calculating S_o. The average S_o decreased if weakly precipitating clouds with low R_p were excluded (Fig. B1, Table B1). It is possible that this was due to the higher N_a and N_c associated with weakly precipitating clouds. The exclusion of weakly-precipitating clouds provides biased trends in S_o

690 since these clouds could have undergone precipitation suppression already. Conversely, strongly precipitating clouds were associated with cleaner conditions and lower N_a and N_c. The exclusion of strongly precipitating clouds also leads to a decrease in the average S_o (Fig. B2, Table B1).

The occurrence of wet scavenging below strongly precipitating clouds (Duong et al., 2011) results in lower below-cloud N_a (and subsequently N_c). Higher susceptibility to precipitation

695 suppression for cleaner, strongly precipitating clouds would explain the increase in the average S_o. This is consistent with observations of S_o using different R_p thresholds (c.f. Fig B1, Jung et al., 2016) and hypotheses regarding the impact of different N_a on S_o (Duong et al., 2011; Fig. 11, Jung et al., 2016).

APPENDIX C – Dependence of S_o on the definition of clean and polluted boundary layers

700 The number of cloud profiles classified into the S-L, C-L, S-H, and C-H regimes varied depending on the below-cloud N_a threshold used to define a low N_a or clean boundary layer. For the threshold used in the base analysis (350 cm^{-3}), contact profiles were more often located in polluted boundary layers (131 out of 171 profiles classified as C-H) while separated profiles were more often located in clean boundary layers (108 out of 148 profiles classified as S-L). The

705 comparisons between S_o in clean and polluted boundary layers varied with the threshold used.

As a sensitivity study, a lower threshold was used to define a clean boundary layer (300 cm^{-3}). For this case, the C-L regime had no profiles in the population with the lowest H ($H < 129$ m) when four populations of profiles were used to examine the dependence of S_o on H. Two out of the other three populations had an insignificant value for S_o due to poor and statistically

710   insignificant correlations between N_c and R_p (Table C1). This was associated with a low sample size for the populations (6 each). A second sensitivity study used a higher threshold to define a clean boundary layer (400 cm^{-3}). For this case, the S-H regime has insignificant S_o for three out of the four populations of H and the remaining population had a small sample size (3 profiles) (Table C1). The base analysis using a threshold of 350 cm^{-3} to define a clean boundary layer was used to

715   compare S_o values that represent a larger number of cloud profiles.

720

725

Atmospheric
Chemistry
and Physics
Discussions

Open Access
EGU

Code availability. University of Illinois/Oklahoma Optical Array Probe (OAP) Processing Software

730   is available at https://doi.org/10.5281/zenodo.1285969 (McFarquhar et al., 2018). The Airborne

Data   Processing   and   Analysis   software   package   is   available   at

https://zenodo.org/record/3733448 (Delene et al., 2020).

Data availability. All ORACLES data are accessible via the digital object identifiers provided under

ORACLES Science Team references: https://doi.org/10.5067/Suborbital/ORACLES/P3/2018_V2

735   (ORACLES Science Team, 2020a), https://doi.org/10.5067/Suborbital/ORACLES/P3/2017_V2

(ORACLES Science Team, 2020b), https://doi.org/10.5067/Suborbital/ORACLES/P3/2016_V2

(ORACLES Science Team, 2020c). ERA5 data were obtained from Climate Data Store (last access:

18 May 2021): https://cds.climate.copernicus.eu/cdsapp#!/home (Hersbach et al., 2020).

Author contributions. GMM and MRP worked with other investigators to design the ORACLES

740   project and flight campaigns. SG designed the study with guidance from GMM. SG analyzed the

data with inputs from GMM, JRO'B, and MRP. JRO'B and DJD processed PCASP data and cloud

probe data, conducted data quality tests, and some of the data comparisons between cloud

probes. SG processed 2D-S and HVPS-3 data and conducted some of the data comparisons

between cloud probes. JDSG processed PDI data. GMM and MRP acquired funding. All authors

745   were involved in data collection during ORACLES. SG wrote the manuscript with guidance from

GMM and reviews from all authors.

Competing interests. The authors declare that they have no conflicts of interest.

765

770

Table 1: The number of cloud profiles (n) for P-3 research flights (PRFs) analyzed in the study, number of contact and separated profiles with sampling time in parentheses, and instruments that provided valid samples of droplets with $D < 50$ μm (instrument used for analysis is in bold).

PRF number and date	n	Contact	Separated	Instruments
PRF05Y16: Sep. 06	24	13 (857 s)	11 (470 s)	**CAS**, PDI
PRF07Y16: Sep. 10	9	0 (0 s)	9 (461 s)	**CAS**, PDI
PRF08Y16: Sep. 12	8	1 (32 s)	7 (472 s)	**CAS**, PDI
PRF09Y16: Sep. 14	8	0 (0 s)	8 (574 s)	**CAS**, PDI
PRF11Y16: Sep. 20	13	13 (669 s)	0 (0 s)	**CAS**, PDI
PRF13Y16: Sep. 25	9	3 (148 s)	6 (363 s)	**CAS**, PDI
PRF01Y17: Aug. 12	15	14 (499 s)	1 (25 s)	CAS, **CDP-B**
PRF02Y17: Aug. 13	17	17 (754 s)	0 (0 s)	CAS, **CDP-B**
PRF03Y17: Aug. 15	12	12 (272 s)	0 (0 s)	CAS, **CDP-B**
PRF04Y17: Aug. 17	7	7 (127 s)	0 (0 s)	CAS, **CDP-B**
PRF07Y17: Aug. 21	13	9 (188 s)	4 (76 s)	CAS, **CDP-B**
PRF08Y17: Aug. 24	9	9 (324 s)	0 (0 s)	CAS, **CDP-B**
PRF10Y17: Aug. 28	11	7 (496 s)	4 (168 s)	CAS, **CDP-B**
PRF01Y18: Sep. 27	21	0 (0 s)	21 (933 s)	CAS, **CDP-B**, CDP-C
PRF02Y18: Sep. 30	13	7 (337 s)	6 (183 s)	CAS, **CDP-B**, CDP-C
PRF04Y18: Oct. 03	5	0 (0 s)	5 (137 s)	CAS, **CDP-B**, CDP-C
PRF05Y18: Oct. 05	4	4 (109 s)	0 (0 s)	CAS, **CDP-B**, CDP-C
PRF06Y18: Oct. 07	10	10 (337 s)	0 (0 s)	CAS, **CDP-B**, CDP-C
PRF07Y18: Oct. 10	13	11 (472 s)	2 (153 s)	**CDP-B**, CDP-C
PRF08Y18: Oct. 12	19	0 (0 s)	19 (773 s)	CDP-B, **CDP-C**
PRF09Y18: Oct. 15	30	17 (766 s)	13 (365 s)	**CDP-B**, CDP-C
PRF11Y18: Oct. 19	12	0 (0 s)	12 (731 s)	CDP-B, **CDP-C**
PRF12Y18: Oct. 21	18	0 (0 s)	18 (833 s)	CDP-B, **CDP-C**
PRF13Y18: Oct. 23	29	19 (777 s)	10 (366 s)	CDP-B, **CDP-C**
Total (2016)	**71**	**30 (1,706 s)**	**41 (2,340 s)**	
Total (2017)	**84**	**75 (2,660 s)**	**9 (269 s)**	
Total (2018)	**174**	**68 (2,798 s)**	**106 (4,474 s)**	
Total	**329**	**173 (7,164 s)**	**156 (7,083 s)**	

775

780

785   Table 2: Range of time, latitude, longitude, Z_T and cloud top pressure (P_T) for PRFs in Table 1.

PRF	Time (UTC)	Latitude (°S)	Longitude (°E)	Z_T (m)	P_T (mb)
PRF05Y16: Sep. 06	08:46 - 12:35	10.2 - 19.7	9.00 - 11.9	359 - 1002	904 - 976
PRF07Y16: Sep. 10	09:09 - 12:36	14.1 - 18.7	4.00 - 8.60	990 - 1201	885 - 908
PRF08Y16: Sep. 12	11:16 - 12:26	9.70 - 12.9	-0.30 - 3.00	1146 - 1226	881 - 890
PRF09Y16: Sep. 14	09:36 - 14:16	16.4 - 18.1	7.50 - 9.00	635 - 824	922 - 945
PRF11Y16: Sep. 20	08:44 - 13:11	15.7 - 17.3	8.90 - 10.5	432 - 636	941 - 966
PRF13Y16: Sep. 25	10:59 - 13:51	10.9 - 14.3	0.80 - 4.30	729 - 1124	890 - 934
PRF01Y17: Aug. 12	11:30 - 15:01	2.41 - 13.0	4.84 - 5.13	748 - 1379	866 - 933
PRF02Y17: Aug. 13	10:15 - 13:07	7.20 - 9.00	4.50 - 5.00	779 - 1384	865 - 928
PRF03Y17: Aug. 15	11:26 - 13.32	9.08 - 15.0	4.96 - 5.00	536 - 1148	887 - 954
PRF04Y17: Aug. 17	12:03 - 16:14	7.99 - 9.43	-7.0 - -12.8	1547 - 1782	827 - 848
PRF07Y17: Aug. 21	13:20 - 16:37	7.96 - 8.05	-8.16 - 3.32	1061 - 1491	855 - 897
PRF08Y17: Aug. 24	11:28 - 14:58	4.90 - 14.8	4.97 - 5.15	911 - 2015	801 - 916
PRF10Y17: Aug. 28	11:46 - 13:18	7.84 - 11.0	4.89 - 5.01	1070 - 1216	881 - 897
PRF01Y18: Sep. 27	10:07 - 13:11	5.66 - 12.1	4.87 - 5.03	819 - 1169	885 - 922
PRF02Y18: Sep. 30	09:50 - 12:24	6.85 - 8.18	4.94 - 5.13	747 - 840	920 - 930
PRF04Y18: Oct. 03	13:17 - 14:41	-1.05 - 4.61	5.00 - 5.06	1137 - 2151	790 - 888
PRF05Y18: Oct. 05	07:22 - 10:09	9.50 - 9.63	5.79 - 6.66	780 - 892	915 - 928
PRF06Y18: Oct. 07	11:04 - 11:29	10.1 - 11.8	5.00 - 5.00	863 - 928	913 - 918
PRF07Y18: Oct. 10	10:16 - 13:31	4.46 - 13.1	4.88 - 5.09	926 - 1329	866 - 912
PRF08Y18: Oct. 12	13:02 - 16:19	1.02 - 4.58	5.50 - 6.96	1073 - 1905	813 - 895
PRF09Y18: Oct. 15	10:27 - 13:09	5.25 - 14.1	4.91 - 5.00	693 - 1547	849 - 937
PRF11Y18: Oct. 19	11:58 - 13:00	6.50 - 7.70	8.00 - 9.06	701 - 1276	873 - 932
PRF12Y18: Oct. 21	10:21 - 13:07	4.91 - 13.5	4.88 - 5.00	675 - 983	902 - 936
PRF13Y18: Oct. 23	10:28 - 13:38	3.07 - 5.00	-2.65 - 5.00	873 - 1281	873 - 915

790

795   Table 3: Average values for cloud properties measured during cloud profiles from the PRFs listed in Table 1 for each *IOP*. Error estimates represent one standard deviation. *R* between *LWP* estimates and *H* in parentheses.

Parameter	2016	2017	2018	All
Profile count	71	84	174	329
N_c (cm^{-3})	150 ± 73	229 ± 108	132 ± 87	157 ± 96
R_e (µm)	7.0 ± 1.9	6.9 ± 1.6	9.8 ± 3.3	8.2 ± 2.7
LWC (g m^{-3})	0.15 ± 0.09	0.21 ± 0.15	0.26 ± 0.17	0.22 ± 0.16
King LWC (g m^{-3})	0.29 ± 0.15	0.23 ± 0.17	0.24 ± 0.14	0.25 ± 0.15
τ	7.2 ± 3.6	7.2 ± 8.9	9.0 ± 7.7	8.8 ± 7.7
H (m)	244 ± 83	148 ± 92	212 ± 116	201 ± 108
LWP (g m^{-2})	34 ± 17 (0.75)	37 ± 43 (0.88)	59 ± 54 (0.83)	48 ± 47 (0.78)
King LWP (g m^{-2})	68 ± 30 (0.80)	37 ± 35 (0.84)	52 ± 40 (0.89)	52 ± 38 (0.87)
LWP_{ad} (g m^{-2})	77 ± 57 (0.97)	51 ± 55 (0.96)	93 ± 97 (0.94)	79 ± 82 (0.93)
C_w (g m^{-3} km^{-1})	2.8 ± 0.3	2.1 ± 0.5	2.4 ± 0.4	2.7 ± 0.3
R_p (mm h^{-1})	0.02 ± 0.05	0.02 ± 0.08	0.10 ± 0.33	0.06 ± 0.25

Table 4: Average and standard deviation for cloud properties measured during contact and
800   separated profiles with 95 % confidence intervals (CIs) from a two-sample t-test applied to contact and separated profile data. Positive CIs indicate higher average for contact profiles and "insignificant" indicates statistically similar averages for contact and separated profiles.

Parameter	Contact	Separated	95 % CIs
N_c (cm^{-3})	200 ± 103	113 ± 63	84 to 90
R_e (µm)	7.5 ± 2.1	9 ± 3	-1.6 to -1.4
τ	8.8 ± 8.3	7 ± 5	0.04 to 3.06
LWC (g m^{-3})	0.23 ± 0.17	0.21 ± 0.14	0.01 to 0.02
CWC (g m^{-3})	0.22 ± 0.16	0.20 ± 0.14	0.01 to 0.02
RWC (x 10^{-3} g m^{-3})	11 ± 15	18 ± 31	-8 to -6
H (m)	194 ± 109	208 ± 106	insignificant
LWP (g m^{-2})	46 ± 49	46 ± 41	insignificant
CWP (g m^{-2})	45 ± 50	46 ± 44	Insignificant
RWP (g m^{-2})	1.8 ± 3.3	3.0 ± 7.1	-2.4 to -0.01
Z_T (m)	1069 ± 267	1004 ± 271	6 to 123
Z_B (m)	874 ± 294	796 ± 274	16 to 140
R_p (mm h^{-1})	0.04 ± 0.09	0.08 ± 0.33	-0.05 to -0.03
S_{AUTO} (x 10^{-10} s^{-1})	1.6 ± 3.0	4.9 ± 12.6	-3.6 to -3.1
S_{ACC} (x 10^{-8} s^{-1})	0.8 ± 1.6	1.7 ± 4.3	-1.1 to -0.8
S_{ACC}/S_{AUTO} (x 10^2)	0.7 ± 1.1	0.5 ± 0.9	0.2 to 0.3

805

Atmospheric
Chemistry
and Physics
Discussions

Table 5: 95 % CIs from statistical comparisons between cloud regimes defined in text.

Parameter	C-H relative to S-H	C-L relative to S-L
Above-cloud N_a (cm^{-3})	852 to 948	387 to 413
Below-cloud N_a (cm^{-3})	194 to 226	45 to 53
N_c (cm^{-3})	98 to 108	25 to 31
R_e (μm)	-1.6 to -1.8	-0.2 to -0.5
R_p (mm h^{-1})	-0.03 to -0.04	0 to -0.04

Table 6: S_o ± standard error for contact, separated, and all profiles, with sample size and R in parentheses. S_o is statistically insignificant if underlined.

H	Contact	Separated	All Profiles
All	0.87 ± 0.04 (173, 0.30)	1.08 ± 0.04 (156, 0.36)	0.88 ± 0.03 (329, 0.33)
28 to 129 m	<u>-0.06 ± 0.11 (52, -0.03)</u>	1.47 ± 0.10 (30, 0.55)	0.67 ± 0.07 (82, 0.28)
129 to 175 m	0.88 ± 0.06 (38, 0.42)	0.53 ± 0.09 (42, 0.20)	0.68 ± 0.05 (80, 0.32)
175 to 256 m	0.92 ± 0.08 (41, 0.27)	0.34 ± 0.07 (44, 0.13)	0.54 ± 0.05 (85, 0.20)
256 to 700 m	1.15 ± 0.06 (42, 0.36)	1.45 ± 0.07 (40, 0.41)	1.13 ± 0.04 (82, 0.40)

810

Table 7: S_o ± standard error with sample size and R in parenthesis for cloud regimes defined in text. S_o is statistically insignificant if underlined.

H	S-L	S-H	C-L	C-H
All	1.29 ± 0.06 (107, 0.40)	0.50 ± 0.06 (41, 0.19)	0.86 ± 0.07 (40, 0.30)	0.33 ± 0.05 (131, 0.11)
28 to 129 m	1.12 ± 0.15 (21, 0.42)	0.43 ± 0.14 (8, 0.27)	<u>0.04 ± 0.42 (4, 0.01)</u>	-0.33 ± 0.11 (48, -0.14)
129 to 175 m	0.66 ± 0.12 (25, 0.25)	0.48 ± 0.18 (11, 0.17)	0.50 ± 0.12 (9, 0.25)	0.26 ± 0.08 (27, 0.13)
175 to 256 m	0.66 ± 0.09 (34, 0.22)	<u>0.07 ± 0.10 (9, 0.03)</u>	1.06 ± 0.13 (14, 0.34)	0.61 ± 0.11 (27, 0.17)
256 to 700 m	1.89 ± 0.09 (27, 0.52)	0.45 ± 0.11 (13, 0.14)	0.72 ± 0.11 (13, 0.24)	0.59 ± 0.09 (29, 0.17)

Table 8: Meteorological and cloud properties from ERA5 reanalysis for contact, separated, and
all profiles with $LCC > 0.95$ (LCC is reported for all profiles), 95 % CIs from a two-sample t-test
applied to contact and separated profile data, and R between each parameter and LWP (R_{LWP})
or H (R_H) with statistically significant R_H and R_{LWP} in bold.

Parameter	Contact	Separated	All	95 % CIs	R_H, R_{LWP}
LCC	0.75 ± 0.29	0.83 ± 0.26	0.79 ± 0.28	-0.14 to -0.02	**0.24**, 0.04
SST (K)	293 ± 2	294 ± 3	293 ± 2	-1.5 to -0	**0.16, 0.22**
H_{BL} (m)	566 ± 164	624 ± 124	600 ± 144	-103 to -11	-0.05, -0.11
ERA5 LWP (g m^{-2})	53 ± 18	51 ± 23	52 ± 21	insignificant	**0.31, 0.18**
ERA5 RWP (g m^{-2})	0.71 ± 1.56	0.32 ± 0.40	0.48 ± 1.07	0.05 to 0.73	**0.19**, -0.01
P_o (mb)	1015 ± 1	1014 ± 2	1014 ± 2	1 to 2	-0.09, -0.07
T_o (K)	293 ± 2	293 ± 3	293 ± 2	insignificant	**0.16, 0.27**
LTS (K)	23 ± 2	22 ± 3	23 ± 3	insignificant	-0.10, **-0.29**
EIS (K)	8.1 ± 1.9	7.8 ± 3.1	7.9 ± 2.7	insignificant	-0.13, **-0.31**

815

Table A1: S_o ± standard error with sample size and R in parentheses for contact, separated, and
all profiles classified into a different number of populations.

H Bin	Contact	Separated	All Profiles
2 populations			
28 to 175 m	0.53 ± 0.05 (90, 0.24)	1.05 ± 0.07 (72, 0.39)	0.69 ± 0.04 (162, 0.30)
175 to 700 m	1.06 ± 0.05 (83, 0.33)	1.02 ± 0.05 (84, 0.33)	0.93 ± 0.03 (167, 0.33)
3 populations			
28 to 145 m	0.08 ± 0.08 (67, 0.04)	1.15 ± 0.09 (41, 0.45)	0.60 ± 0.05 (108, 0.26)
145 to 224 m	0.95 ± 0.07 (51, 0.34)	0.25 ± 0.06 (60, 0.11)	0.60 ± 0.04 (111, 0.25)
224 to 700 m	1.08 ± 0.05 (55, 0.34)	1.45 ± 0.06 (55, 0.41)	1.05 ± 0.04 (110, 0.37)

Table B1: S_o ± standard error with sample size and R in parentheses for contact, separated, and
all profiles with R_p above a certain threshold.

H Bin	Contact	Separated	All Profiles
$R_p > 10^{-3}$ mm h^{-1}			
All	0.88 ± 0.03 (173, 0.34)	0.95 ± 0.04 (156, 0.36)	0.84 ± 0.02 (329, 0.37)
28 to 129 m	0.03 ± 0.10 (52, 0.02)	1.41 ± 0.09 (30, 0.61)	0.71 ± 0.07 (82, 0.33)
129 to 175 m	0.94 ± 0.05 (38, 0.49)	0.64 ± 0.09 (42, 0.27)	0.78 ± 0.04 (80, 0.40)
175 to 256 m	0.78 ± 0.07 (41, 0.30)	0.21 ± 0.06 (44, 0.10)	0.38 ± 0.04 (85, 0.18)
256 to 700 m	1.11 ± 0.06 (42, 0.38)	1.18 ± 0.07 (40, 0.39)	1.06 ± 0.04 (82, 0.42)
$R_p > 10^{-2}$ mm h^{-1}			
All	0.49 ± 0.03 (173, 0.27)	0.76 ± 0.03 (156, 0.38)	0.61 ± 0.02 (329, 0.35)
28 to 129 m	0.01 ± 0.08 (52, 0.01)	0.97 ± 0.10 (30, 0.57)	0.48 ± 0.06 (82, 0.36)
129 to 175 m	0.70 ± 0.04 (38, 0.53)	0.53 ± 0.08 (42, 0.29)	0.66 ± 0.04 (80, 0.44)
175 to 256 m	0.62 ± 0.06 (41, 0.31)	0.48 ± 0.05 (44, 0.31)	0.47 ± 0.04 (85, 0.28)
256 to 700 m	0.37 ± 0.05 (42, 0.19)	0.78 ± 0.06 (40, 0.33)	0.60 ± 0.03 (82, 0.32)

Table C1: S_o ± standard error with sample size and R in parenthesis for regimes defined in text
and different thresholds to define a low N_a boundary layer. S_o is statistically insignificant if
underlined.

H	S-L	S-H	C-L	C-H
Low N_a = 300 cm^{-3}				
All	1.37 ± 0.06 (96, 0.42)	0.45 ± 0.06 (52, 0.17)	0.29 ± 0.10 (21, 0.10)	0.84 ± 0.04 (150, 0.29)
28 to 129 m	1.20 ± 0.16 (19, 0.44)	0.38 ± 0.13 (10, 0.25)	NaN (0, NaN)	<u>-0.06 ± 0.11 (52, -0.03)</u>
129 to 175 m	0.68 ± 0.13 (21, 0.26)	0.56 ± 0.16 (15, 0.20)	<u>0.02 ± 0.15 (6, 0.01)</u>	0.86 ± 0.07 (30, 0.41)
175 to 256 m	0.70 ± 0.10 (31, 0.24)	<u>0.07 ± 0.10 (12, 0.03)</u>	0.44 ± 0.17 (9, 0.15)	1.04 ± 0.10 (32, 0.30)
256 to 700 m	2.03 ± 0.10 (25, 0.55)	0.40 ± 0.10 (15, 0.12)	<u>-0.09 ± 0.17 (6, -0.03)</u>	1.13 ± 0.07 (36, 0.36)
Low N_a = 400 cm^{-3}				
All	1.12 ± 0.05 (125, 0.36)	0.37 ± 0.09 (23, 0.16)	1.11 ± 0.05 (64, 0.39)	0.25 ± 0.06 (107, 0.08)
28 to 129 m	1.04 ± 0.13 (23, 0.43)	<u>-0.20 ± 0.21 (6, -0.11)</u>	0.51 ± 0.22 (11, 0.21)	-0.33 ± 0.13 (41, -0.14)
129 to 175 m	0.81 ± 0.11 (30, 0.30)	<u>0.02 ± 0.19 (6, 0.01)</u>	0.90 ± 0.10 (12, 0.43)	0.22 ± 0.09 (24, 0.10)
175 to 256 m	0.53 ± 0.09 (35, 0.19)	<u>0.12 ± 0.12 (8, 0.06)</u>	0.84 ± 0.09 (24, 0.30)	0.53 ± 0.19 (17, 0.12)
256 to 700 m	1.42 ± 0.07 (37, 0.41)	1.10 ± 0.42 (3, 0.25)	1.52 ± 0.08 (17, 0.50)	0.47 ± 0.09 (25, 0.13)
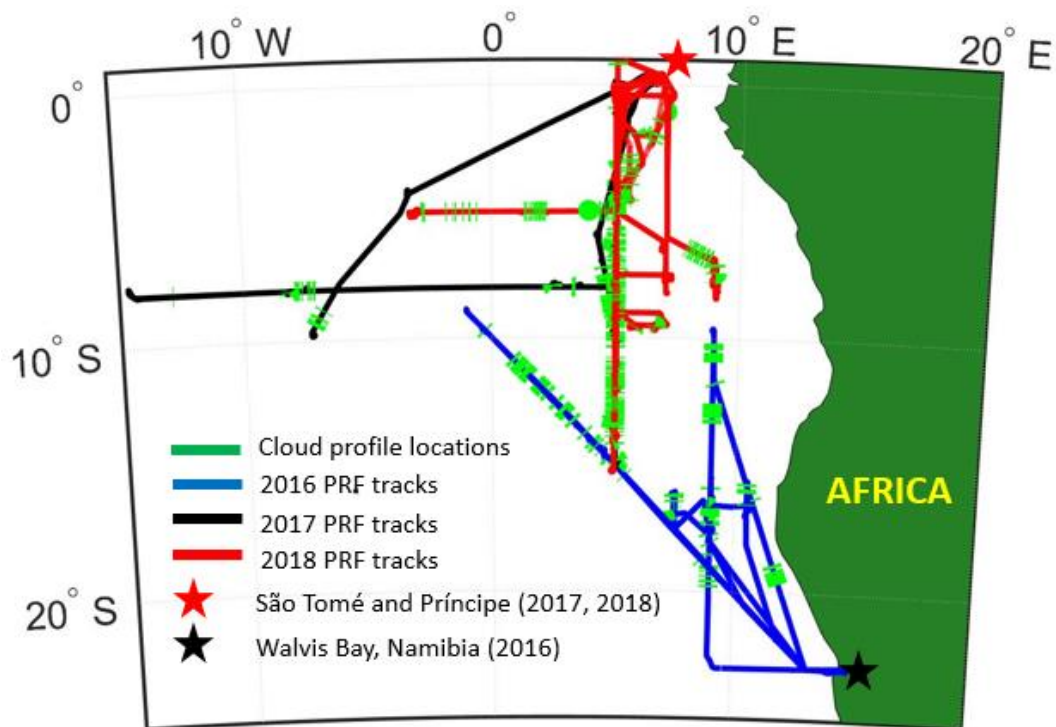
Figure 1: PRF tracks from ORACLES IOPs with base of operations and cloud sampling locations (tracks for multiple 2017 and 2018 PRFs overlap along 5° E).
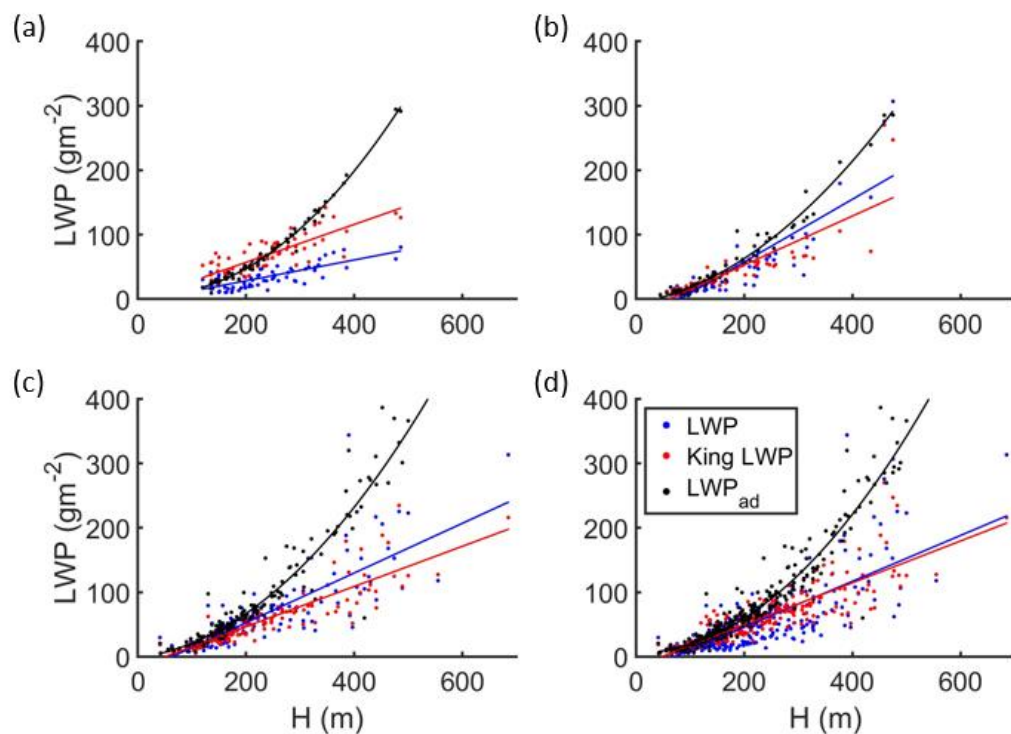
Atmospheric
Chemistry
and Physics
Discussions
Open Access
EGU

Figure 2: LWP from size-resolved probes, King LWP from the hot-wire, and adiabatic LWP (LWP$_{ad}$) for profiles with LWP_{ad} > 5 g m^{-2} as a function of H for (a) 2016, (b) 2017, (c) 2018, and 835 (d) all years with best-fit curves from a regression model applied to each LWP versus H.
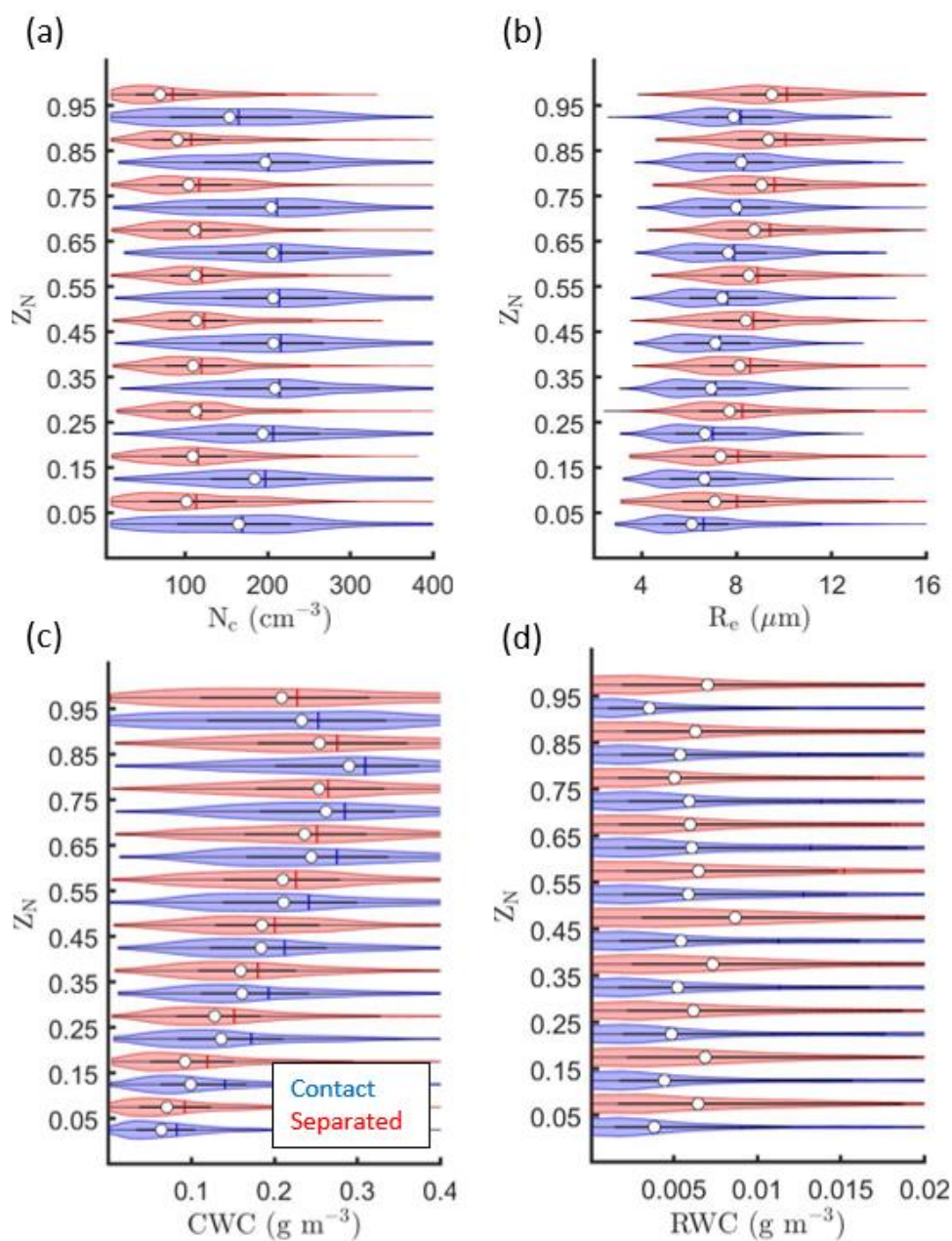
Figure 3: Kernel density estimates (indicated by the width of shaded area) and boxplots showing the 25th, 50th (white circle), and 75th percentiles for (a) N_c, (b) R_e, (c) CWC, and (d) RWC as a function of Z_N for contact and separated profiles.
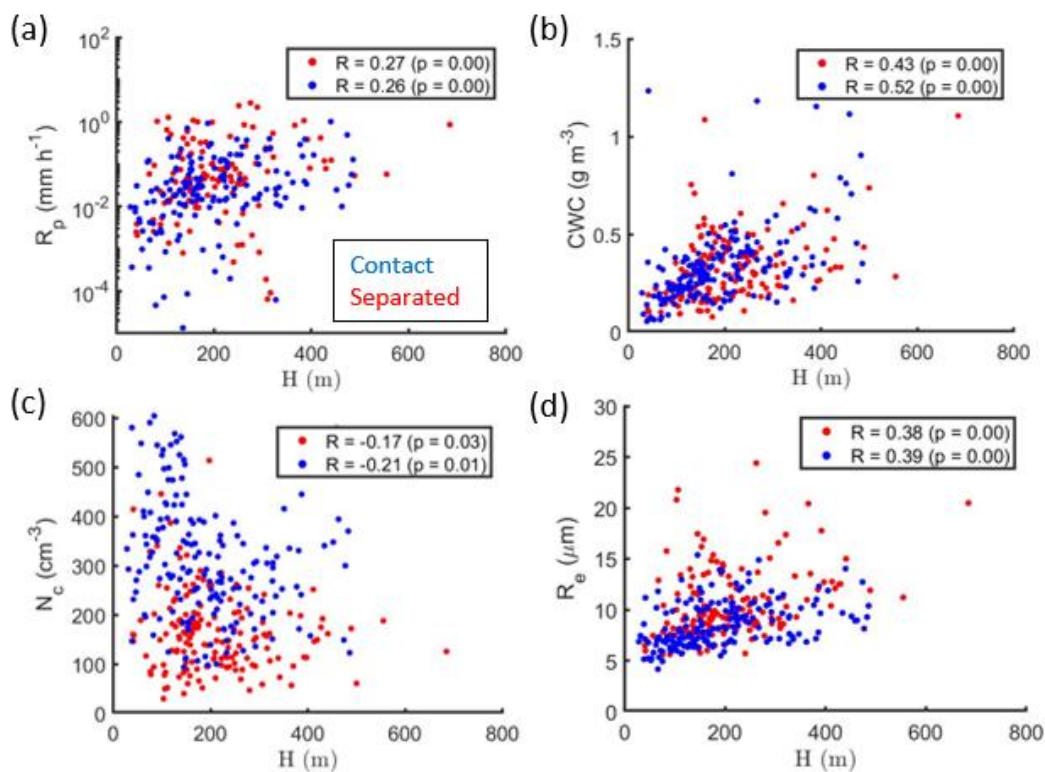
840

Figure 4: The 95th percentile for (a) R_p, (b) CWC, (c) N_c, and (d) R_e as a function of H. Each dot represents the 95th percentile from the 1 Hz measurements for a single cloud profile. Pearson's correlation coefficient (R) and p-value for the correlation indicated in legend.
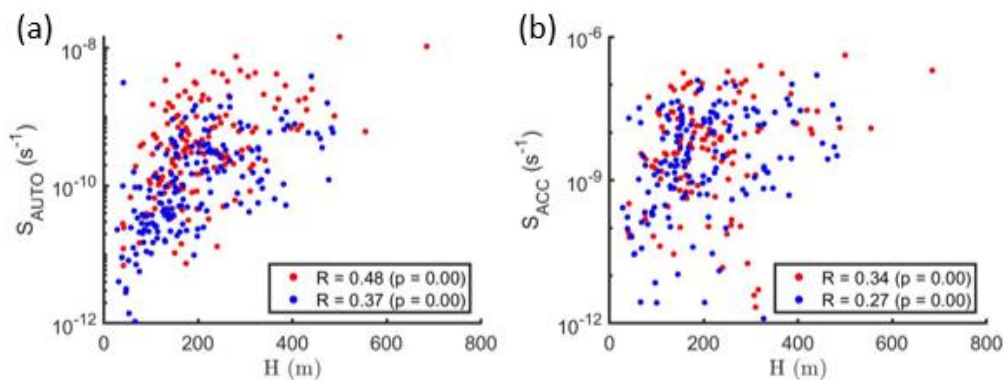
845

Figure 5: The 95th percentile for (a) S_{AUTO} and (b) S_{ACC} as a function of H. Each dot represents the 95th percentile from the 1 Hz measurements for a single cloud profile. R and p-value for the correlation indicated in legend.
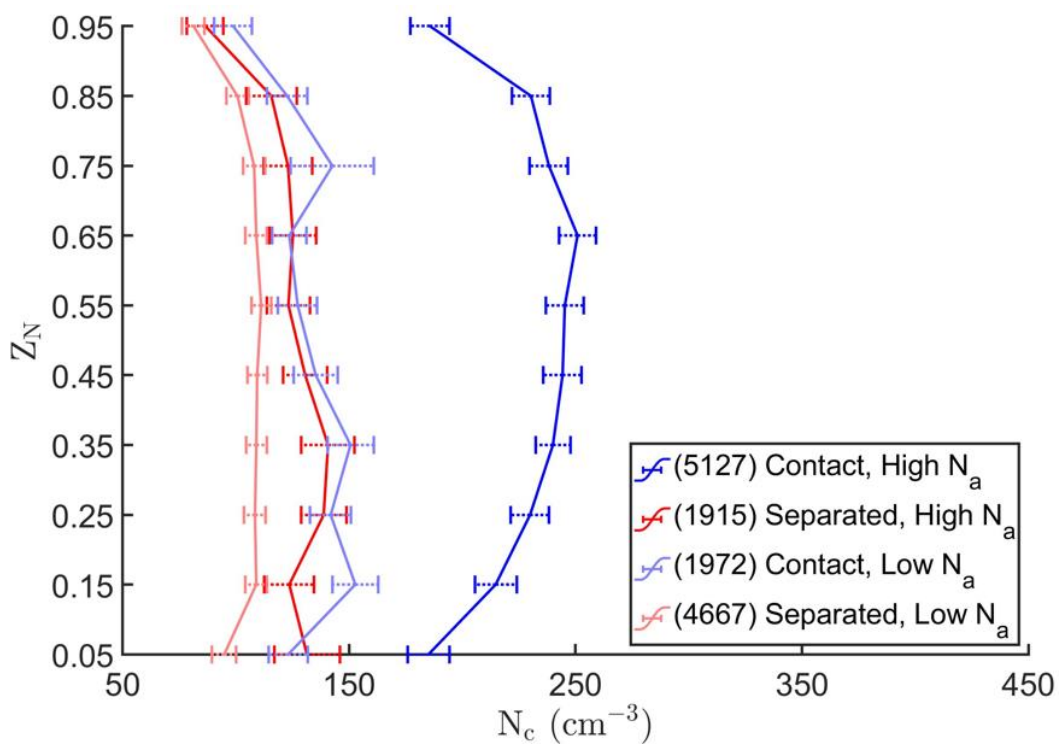
Figure 6: Average N_c (error bars extend to 95 % CIs) as a function of Z_N. Number of 1 Hz data points and corresponding regimes indicated in legend.
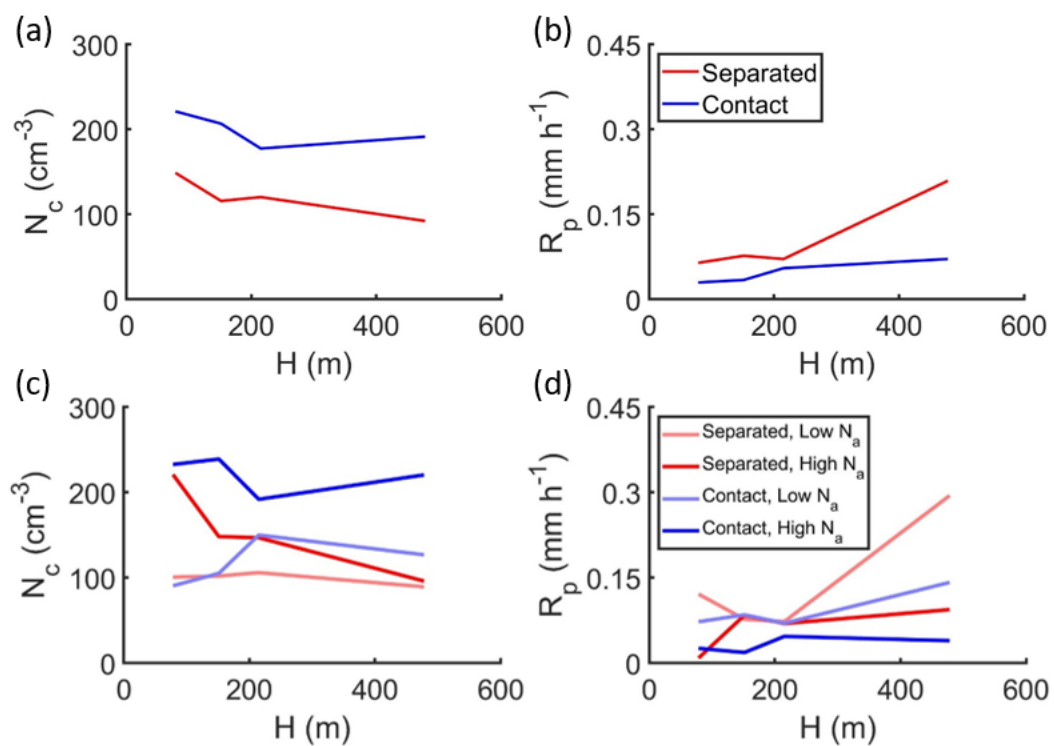
Figure 7: The average (a, c) N_c and (b, d) R_p as a function of H for (a, b) contact and separated profiles, and (c, d) the regimes indicated in legend.

855
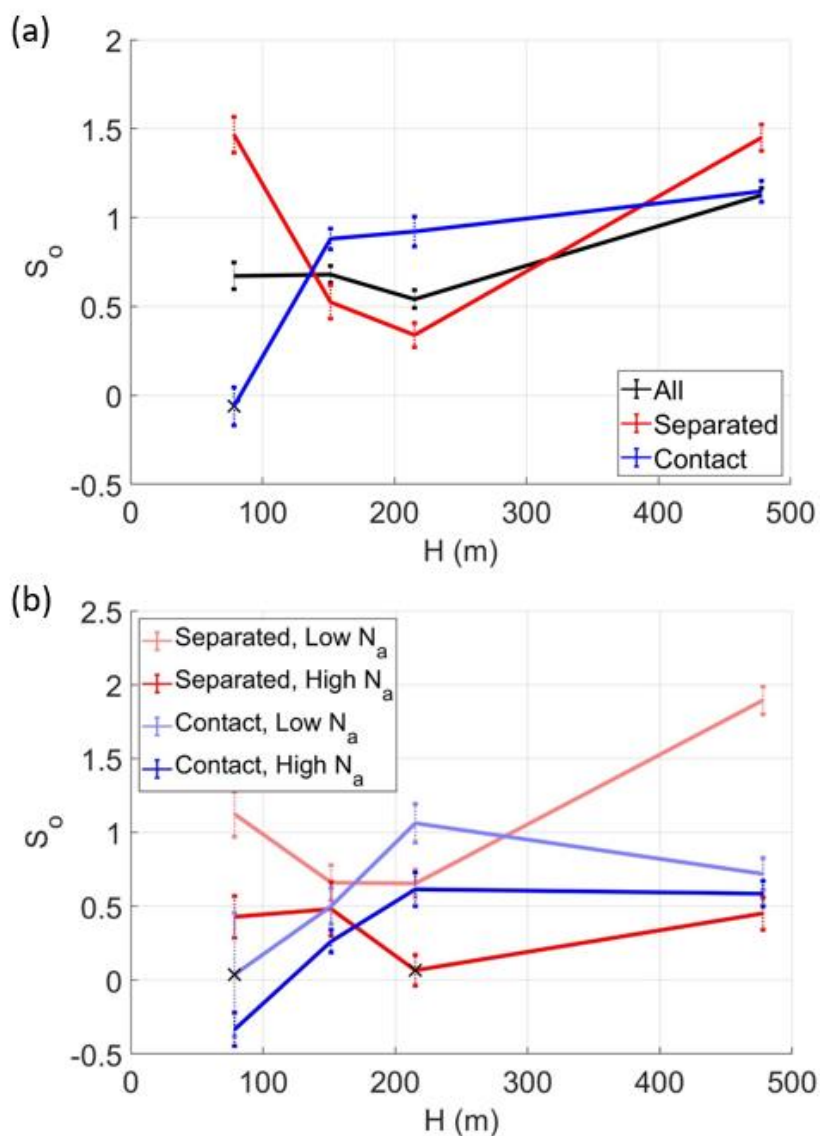
Figure 8: S_o as a function of H (error bars extend to standard error from the regression model) for (a) contact, separated, and all profiles, and (b) the regimes indicated in legend. S_o was statistically insignificant when marked with a cross.

Atmospheric
Chemistry
and Physics
Discussions

Open Access

EGU
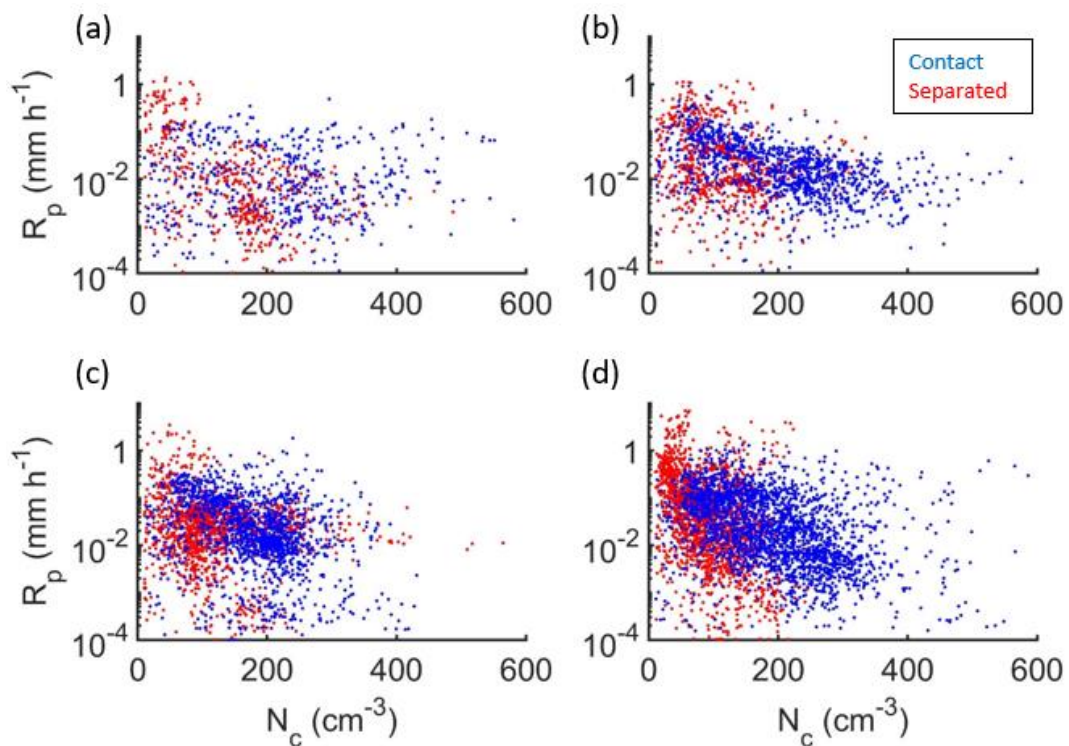
860   Figure 9: Scatter plots of R_p and N_c for 1 Hz data points from contact and separated profiles with
(a) 28 < H < 129 m, (b) 129 < H < 175 m, (c) 175 < H < 256 m, and (d) 256 < H < 700 m.

865
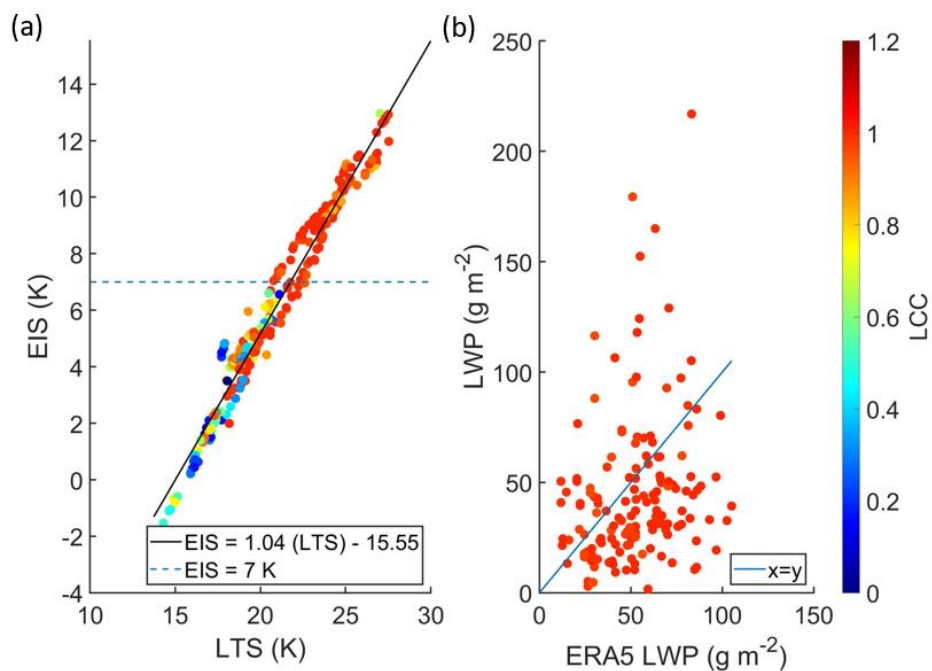
Figure 10: (a) LTS versus EIS with regression coefficients in legend (R = 0.98) and (b) LWP from
size-resolved probes versus LWP from the ERA5 reanalysis (R = 0.18) where each dot represents
a single cloud profile. LTS, EIS, ERA5 LWP, and LCC for each cloud profile taken from the nearest
ERA5 grid box (within 0.25° of latitude and longitude) at 12:00 UTC. Panel (a) shows all cloud
profiles and panel (b) shows cloud profiles with LCC > 0.95.
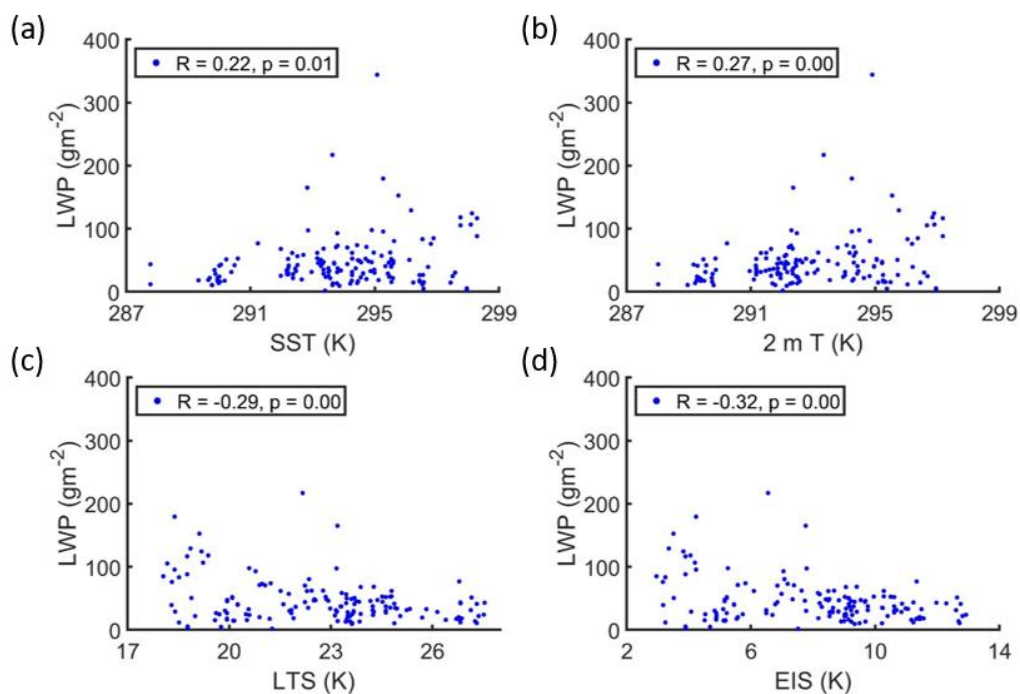
Figure 11: LWP from size-resolved probes as a function of (a) SST, (b) 2 m *T*, (c) LTS, and (d) EIS. Each dot represents a single cloud profile with LCC > 0.95 and SST, 2 m *T*, LTS, and EIS taken from the nearest ERA5 grid box (within 0.25˚ of latitude and longitude) at 12:00 UTC.
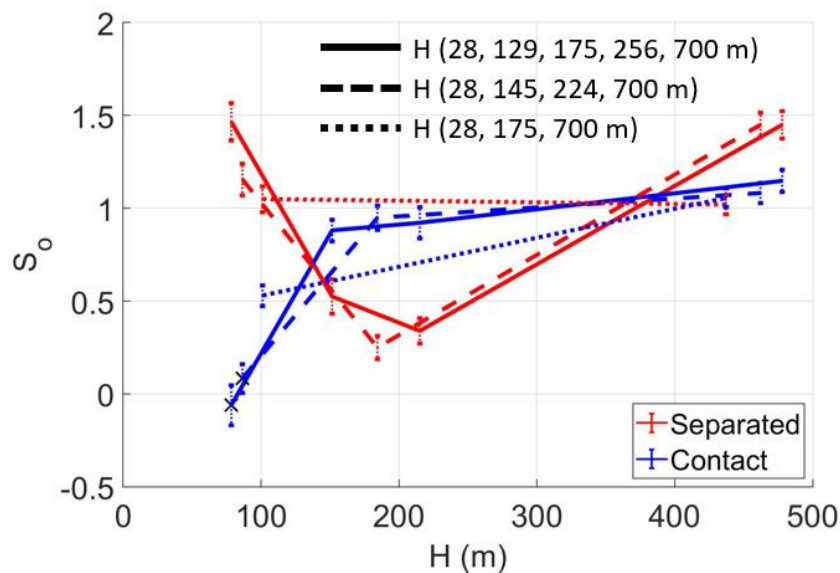
Figure A1: S_o as a function of H for contact and separated profiles classified into different populations using the end points indicated in legend. S_o was statistically insignificant when marked with a cross.
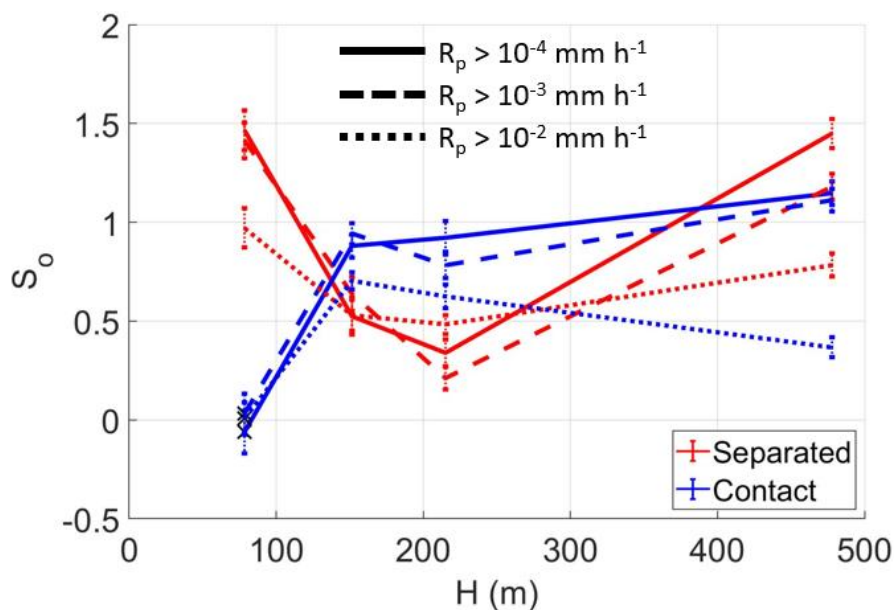
Figure B1: S_o as a function of H for contact and separated profiles with R_p greater than the thresholds indicated in legend. S_o was statistically insignificant when marked with a cross.
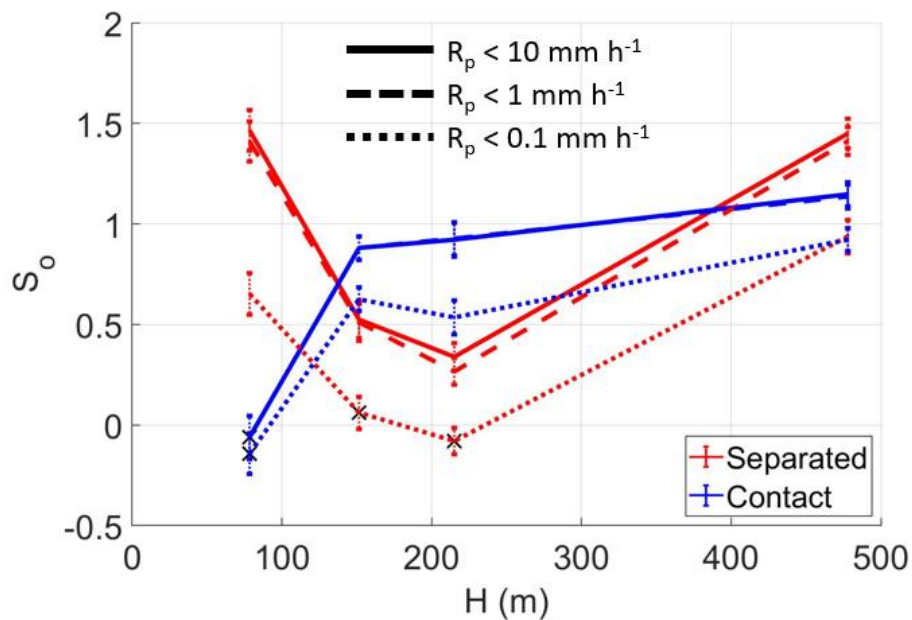
Figure B2: S_o as a function of H for contact and separated profiles with R_p less than the thresholds indicated in legend. S_o was statistically insignificant when marked with a cross.

890

895

900

Atmospheric
Chemistry
and Physics
Discussions

REFERENCES:

Abel, S. J. and Boutle, I. A.: An improved representation of the raindrop size distribution for single-moment microphysics schemes, Q. J. Roy. Meteorol. Soc., 138, 2151–2162, https://doi.org/10.1002/qj.1949, 2012.

Ackerman, A. S., Kirkpatrick, M. P., Stevens, D. E., and Toon, O. B.: The impact of humidity above stratiform clouds on indirect aerosol climate forcing, Nature, 432, 1014–1017, 2004.

Ackerman, A. S., Toon, O. B., Stevens, D. E., Heymsfield, A. J., Ramanathan, V., and Welton, E. J.: Reduction of tropical cloudiness by soot, Science, 288, 1042–1047, 2000.

Adebiyi, A. A. and Zuidema, P.: The role of the southern African easterly jet in modifying the southeast Atlantic aerosol and cloud environments, Q. J. Roy. Meteor. Soc., 142, 1574–1589, https://doi.org/10.1002/qj.2765, 2016.

Afchine, A., Rolf, C., Costa, A., Spelten, N., Riese, M., Buchholz, B., Ebert, V., Heller, R., Kaufmann, S., Minikin, A., Voigt, C., Zöger, M., Smith, J., Lawson, P., Lykov, A., Khaykin, S., and Krämer, M.: Ice particle sampling from aircraft – influence of the probing position on the ice water content, Atmos. Meas. Tech., 11, 4015–4031, https://doi.org/10.5194/amt-11-4015-2018, 2018.

Ahlgrimm M, Randall DA, Kohler M.. Evaluating cloud frequency of ¨ occurrence and cloud-top height using spaceborne lidar observations. Mon. Weather Rev. 137: 4225–4237, 2009.

Ahlgrimm, M. and Forbes, R.: Improving the Representation of Low Clouds and Drizzle in the ECMWF Model Based on ARM Observations from the Azores, Mon. Weather Rev., 142, 668– 685, doi:10.1175/mwr-d-13-00153.1, 2014.

Albrecht, B.: Aerosols, Cloud Microphysics, and Fractional Cloudiness, Science, 245, 1227–1230,

925   1989.

Bai, H., Gong, C., Wang, M., Zhang, Z., and L'Ecuyer, T.: Estimating precipitation susceptibility in

warm marine clouds using multi-sensor aerosol and cloud products from A-Train

satellites, Atmos. Chem. Phys., 18, 1763–1783, https://doi.org/10.5194/acp-18-1763-

2018, 2018.

930   Behrangi, A., Stephens, G., Adler, R. F., Huffman, G. J., Lambrigtsen, B., and Lebsock, M.: An

update on the oceanic precipitation rate and its zonal distribution in light of advanced

observations from space, J. Climate, 27, 3957–3965, https://doi.org/10.1175/JCLI-D-13-

00679.1, 2014.

Bennartz, R.: Global assessment of marine boundary layer cloud droplet number concentration

935   from satellite, J. Geophys. Res., 112, D02201, doi:10.1029/2006JD007547, 2007.

Boers, R., Acarreta, J. R., and Gras, J. L.: Satellite monitoring of the first indirect aerosol effect:

Retrieval of the droplet concentration of water clouds, J. Geophys. Res.-Atmos., 111,

D22208, https://doi.org/10.1029/2005JD006838, 2006.

Bony, S. and Dufrense, J.-L.: Marine boundary layer clouds at the heart of tropical feedback

940   uncertainties   in   climate   models,   Geophys.   Res.   Lett.,   32,   L20806,

doi:10.1029/2005GL023851, 2005.

Boucher, O., Randall, D., Artaxo, P., Bretherton, C., Feingold, G., Forster, P., Kerminen, V.-M.,

Kondo, Y., Liao, H., Lohmann, U., Rasch, P., Satheesh, S. K., Sherwood, S., Stevens, B., and

Zhang, X. Y.: Clouds and Aerosols. In: Climate Change 2013: The Physical Science Basis,

945   Contribution of Working Group I to the Fifth Assessment Report of the Intergovernmental

Panel on Climate Change, edited by: Stocker, T. F., Qin, D., Plattner, G.-K., Tignor, M., Allen, S. K., Boschung, J., Nauels, A., Xia, Y., Bex, V., and Midgley, P. M., Cambridge University Press, Cambridge, United Kingdom and New York, NY, USA, 571–657, 2013.

Boutle, I. A., Abel, S. J., Hill, P. G., and Morcrette, C. J.: Spatial variability of liquid cloud and rain:
950   observations and microphysical effects, Q. J. Roy. Meteorol. Soc., 140, 583–594, https://doi.org/10.1002/qj.2140, 2014.

Braun, R. A., Dadashazar, H., MacDonald, A. B., Crosbie, E., Jonsson, H. H., Woods, R. K., Flagan, R. C., Seinfeld, J. H., and Sorooshian, A.: Cloud Adiabaticity and Its Relationship to Marine Stratocumulus Characteristics Over the Northeast Pacific Ocean, J. Geophys. Res.-Atmos.,
955   123, 13790–13806, https://doi.org/10.1029/2018JD029287, 2018.

Brenguier, J.-L., Pawlowska, H., Schuller, L., Preusker, R., Fischer, J., and Fouquart, Y.: Radiative properties of boundary layer clouds: Droplet effective radius versus number concentration, J. Atmos. Sci., 57, 803-821, 2000.

Chen, Y.-C., Christensen, M. W., Stephens, G. L., and Seinfeld, J. H.: Satellite-based estimate of
960   global aerosol–cloud radiative forcing by marine warm clouds, Nat. Geosci., 7, 643–646, doi:10.1038/ngeo2214, 2014.

Christensen, M. W. and Stephens, G. L.: Microphysical and macrophysical responses of marine stratocumulus polluted by underlying ships. Part 2: Impacts of haze on precipitating clouds, J. Geophys. Res., 117, D11203, doi:10.1029/2011JD017125, 2012

965   Cochrane, S. P., Schmidt, K. S., Chen, H., Pilewskie, P., Kittelman, S., Redemann, J., LeBlanc, S., Pistone, K., Kacenelenbogen, M., Segal Rozenhaimer, M., Shinozuka, Y., Flynn, C., Platnick, S., Meyer, K., Ferrare, R., Burton, S., Hostetler, C., Howell, S., Freitag, S., Dobracki, A., and

Doherty, S.: Above-cloud aerosol radiative effects based on ORACLES 2016 and ORACLES

2017 aircraft experiments, Atmos. Meas. Tech., 12, 6505–6528,

970 https://doi.org/10.5194/amt-12-6505-2019, 2019.

CDS, ERA5: Fifth generation of ECMWF atmospheric reanalyses of the global climate,

https://cds.climate.copernicus. eu/cdsapp#!/home, accessed 2019-11-26, 2017.

Coddington, O., Pilewskie, P., Redemann, J., Platnick, S., Russell, P., Schmidt, K., Gore, W.,

Livingston, J., Wind, G., and Vukicevic, T.: Examining the impact of overlying aerosols on

975 the retrieval of cloud optical properties from passive remote sensing, J. Geophys. Res.,

115, D10211, doi:10.1029/2009JD012829, 2010.

Diamond, M. S., Dobracki, A., Freitag, S., Small Griswold, J. D., Heikkila, A., Howell, S. G., Kacarab,

M. E., Podolske, J. R., Saide, P. E., and Wood, R.: Time-dependent entrainment of smoke

presents an observational challenge for assessing aerosol–cloud interactions over the

980 southeast Atlantic Ocean, Atmos. Chem. Phys., 18, 14623–14636,

https://doi.org/10.5194/acp-18- 14623-2018, 2018.

Delene, D. J.: Airborne Data Processing and Analysis Software Package, Earth Science Informatics,

4(1), 29-44, 2011.

Devasthale, A. and Thomas, M. A.: A global survey of aerosol-liquid water cloud overlap based on

985 four years of CALIPSO-CALIOP data, Atmos. Chem. Phys., 11, 1143–1154,

https://doi.org/10.5194/acp-11-1143-2011, 2011.

Doherty, S. J., Saide, P. E., Zuidema, P., Shinozuka, Y., Ferrada, G. A., Gordon, H., Mallet, M.,

Meyer, K., Painemal, D., Howell, S. G., Freitag, S., Dobracki, A., Podolske, J. R., Burton, S.

P., Ferrare, R. A., Howes, C., Nabat, P., Carmichael, G. R., da Silva, A., Pistone, K., Chang,

990   I., Gao, L., Wood, R., and Redemann, J.: Modeled and observed properties related to the

direct aerosol radiative effect of biomass burning aerosol over the Southeast Atlantic,

Atmos. Chem. Phys. Discuss. [preprint], https://doi.org/10.5194/acp-2021-333, in review,

2021.

Douglas, A. and L'Ecuyer, T.: Quantifying variations in shortwave aerosol–cloud–radiation

995   interactions using local meteorology and cloud state constraints, Atmos. Chem. Phys., 19,

6251–6268, https://doi.org/10.5194/acp-19-6251-2019, 2019.

Douglas, A. and L'Ecuyer, T.: Quantifying cloud adjustments and the radiative forcing due to

aerosol–cloud interactions in satellite observations of warm marine clouds, Atmos. Chem.

Phys., 20, 6225–6241, https://doi.org/10.5194/acp-20-6225-2020, 2020.

1000   Duong, H. T., Sorooshian, A., and Feingold, G.: Investigating potential biases in observed and

modeled metrics of aerosol-cloud-precipitation interactions, Atmos. Chem. Phys., 11,

4027–4037, https://doi.org/10.5194/acp-11-4027-2011, 2011.

Dzambo, A. M., L'Ecuyer, T. S., Sy, O. O., and Tanelli, S.: The Observed Structure and Precipitation

Characteristics of Southeast Atlantic Stratocumulus from Airborne Radar during ORACLES

1005   2016–17, J. Appl. Meteor. Climatol., 58, 2197–2215, https://doi.org/10.1175/JAMC-D-

19-0032.1, 2019.

Dzambo, A. M., L'Ecuyer, T., Sinclair, K., van Diedenhoven, B., Gupta, S., McFarquhar, G., O'Brien,

J. R., Cairns, B., Wasilewski, A. P., and Alexandrov, M.: Joint cloud water path and

rainwater path retrievals from airborne ORACLES observations, Atmos. Chem. Phys., 21,

1010   5513–5532, https://doi.org/10.5194/acp-21-5513-2021, 2021.

Eastman, R., Warren, S. G., and Hahn, C. J.: Variations in Cloud Cover and Cloud Types over the Ocean from Surface Observations, 1954–2008, J. Clim., 24, 5914–5934, doi:10.1175/2011JCLI3972.1, 2011.

Feingold, G. and Siebert, H.: Cloud – Aerosol Interactions from the Micro to the Cloud Scale, from the Strungmann Forum Report, Clouds in the Perturbed Climate System: Their Relationship to Energy Balance, Atmospheric Dynamics, and Precipitation, edited by: Heintzenberg, J. and Charlson, R. J., MIT Press, ISBN 978-0-262-01287-4, 2009.

Gettelman, A., Morrison, H., Terai, C. R., and Wood, R.: Microphysical process rates and global aerosol–cloud interactions, Atmos. Chem. Phys., 13, 9855–9867, doi:10.5194/acp-13-9855-2013, 2013.

Geoffroy, O., Brenguier, J.-L., and Burnet, F.: Parametric representation of the cloud droplet spectra for LES warm bulk microphysical schemes, Atmos. Chem. Phys., 10, 4835–4848, doi:10.5194/acp-10-4835-2010, 2010.

Geoffroy, O., Brenguier, J.-L., and Sandu, I.: Relationship between drizzle rate, liquid water path and droplet concentration at the scale of a stratocumulus cloud system, Atmos. Chem. Phys., 8, 4641–4654, doi:10.5194/acp-8-4641-2008, 2008.

Gordon, H., Field, P. R., Abel, S. J., Dalvi, M., Grosvenor, D. P., Hill, A. A., Johnson, B. T., Miltenberger, A. K., Yoshioka, M., and Carslaw, K. S.: Large simulated radiative effects of smoke in the south-east Atlantic, Atmos. Chem. Phys., 18, 15261–15289, https://doi.org/10.5194/acp-18-15261-2018, 2018.

Grosvenor, D. P., Sourdeval, O., Zuidema, P., Ackerman, A., Alexandrov, M. D., Bennartz, R., Boers, R., Cairns, B., Chiu, J. C., Christensen, M., Deneke, H., Diamond, M., Feingold, G.,

1015

1020

1025

1030

Fridlind, A., Hünerbein, A., Knist, C., Kollias, P., Marshak, A., McCoy, D., Merk, D., Painemal, D., Rausch, J., Rosenfeld, D., Russchenberg, H., Seifert, P., Sinclair, K., Stier, P.,
1035   van Diedenhoven, B., Wendisch, M., Werner, F., Wood, R., Zhang, Z., and Quaas, J.: Remote Sensing of Droplet Number Concentration in Warm Clouds: A Review of the Current State of Knowledge and Perspectives, Rev. Geophys., 56, 409–453, https://doi.org/10.1029/2017RG000593, 2018.

Gryspeerdt, E., Goren, T., Sourdeval, O., Quaas, J., Mülmenstädt, J., Dipu, S., Unglaub, C.,
1040   Gettelman, A., and Christensen, M.: Constraining the aerosol influence on cloud liquid water path, Atmos. Chem. Phys., 19, 5331–5347, https://doi.org/10.5194/acp-19-5331-2019, 2019.

Gupta, S., McFarquhar, G. M., O'Brien, J. R., Delene, D. J., Poellot, M. R., Dobracki, A., Podolske, J. R., Redemann, J., LeBlanc, S. E., Segal-Rozenhaimer, M., and Pistone, K.: Impact of the
1045   variability in vertical separation between biomass burning aerosols and marine stratocumulus on cloud microphysical properties over the Southeast Atlantic, Atmos. Chem. Phys., 21, 4615–4635, https://doi.org/10.5194/acp-21-4615-2021, 2021.

Hannay, C., Williamson, D., Hack, J., Kiehl, J., Olson, J., Klein, S., Bretherton, C., and Kohler, M.: Evaluation of forecasted south-¨ east pacific stratocumulus in the NCAR, GFDL, and
1050   ECMWF Models, J. Climate, 22, 2871–2889, 2009.

Hansen, J. and Travis, L. D.: Light scattering in planetary atmospheres, Space Sci. Rev., 16, 527–610, 1974

Hersbach, H., Bell, B., Berrisford, P., Hirahara, S., Horányi, A., Muñoz-Sabater, J., Nicolas, J., Peubey, C., Radu, R., Schepers, D., Simmons, A., Soci, C., Abdalla, S., Abellan, X., Balsamo,

Atmospheric
Chemistry
and Physics
Discussions

1055   G., Bechtold, P., Biavati, G., Bidlot, J., Bonavita, M., De Chiara, G., Dahlgren, P., Dee, D., Diamantakis, M., Dragani, R., Flemming, J., Forbes, R., Fuentes, M., Geer, A., Haimberger, L., Healy, S., Hogan, R. J., Hólm, E., Janisková, M., Keeley, S., Laloyaux, P., Lopez, P., Lupu, C., Radnoti, G., de Rosnay, P., Rozum, I., Vamborg, F., Villaume, S., and Thépaut, J.-N.: The ERA5 Global Reanalysis, Q. J. Roy. Meteor. Soc., 146, 730, 1999– 2049,

1060   https://doi.org/10.1002/qj.3803, 2020.

Hill, A. A., Dobbie, S., and Yin, Y.: The impact of aerosols on non-precipitating marine stratocumulus. Model description and prediction of the indirect effect, Q. J. Roy. Meteorol. Soc., 134, 1143–1154, doi:10.1002/qj.278, 2008.

IFS Documentation CY47R1: IFS Documentation CY47R1 – Part IV: Physical Processes, ECMWF,

1065   doi:10.21957/cpmkqvhja

Janssen, R. H. H., Ganzeveld, L. N., Kabat, P., Kulmala, M., Nieminen, T., and Roebeling, R. A.: Estimating seasonal variations in cloud droplet number concentration over the boreal forest from satellite observations, Atmos. Chem. Phys., 11, 7701–7713, https://doi.org/10.5194/acp-11-7701-2011, 2011.

1070 Jiang, H., Feingold, G., and Sorooshian, A.: Effect of aerosol on the susceptibility and efficiency of precipitation in trade cumulus clouds, J. Atmos. Sci., 67, 3525–3540, 2010.

Johnson, B. T., Shine, K. P., and Forster, P. M.: The semi-direct aerosol effect: Impact of absorbing aerosols on marine stratocumulus, Q. J. R. Meteorol. Soc., 130, 1407–1422, 2004.

Jung, E., Albrecht, B. A., Sorooshian, A., Zuidema, P., and Jonsson, H. H.: Precipitation

1075   susceptibility in marine stratocumulus and shallow cumulus from airborne

measurements, Atmos. Chem. Phys., 16, 11395–11413, https://doi.org/10.5194/acp-16-11395-2016, 2016.

Khairoutdinov, M. and Kogan, Y.: A new cloud physics parameterization in a large-eddy simulation model of marine stratocumulus, Mon. Weather Rev., 128, 229–243, 2000.

1080   Klein, S. A. and Hartmann, D. L.: The seasonal cycle of low stratiform clouds, J. Climate, 6, 1587–1606, 1993.

Köhler, M., Ahlgrimm, M., and Beljaars, A.: Unified treatment of dry convective and stratocumulus-topped boundary layers in the ECMWF model, Q. J. Roy. Meteor. Soc., 137, 43–57, 2011.

1085   Kubar, T. L., Hartmann, D. L., and Wood, R.: Understanding the importance of microphysics and macrophysics for warm rain in marine low clouds. Part I: Satellite observations, J. Atmos. Sci. 66, 2953–2972, 2009.

Lawrence, M. G.: The relationship between relative humidity and the dewpoint temperature in moist air: A simple conversion and applications, Bull. Am. Met. Soc., 86, 225–233, 2005.

1090   LeBlanc, S. E., Redemann, J., Flynn, C., Pistone, K., Kacenelenbogen, M., Segal-Rosenheimer, M., Shinozuka, Y., Dunagan, S., Dahlgren, R. P., Meyer, K., Podolske, J., Howell, S. G., Freitag, S., Small-Griswold, J., Holben, B., Diamond, M., Wood, R., Formenti, P., Piketh, S., Maggs-Kölling, G., Gerber, M., and Namwoonde, A.: Above-cloud aerosol optical depth from airborne observations in the southeast Atlantic, Atmos. Chem. Phys., 20, 1565–1590,
1095   https://doi.org/10.5194/acp-20-1565-2020, 2020.

Mauger, G. S. and Norris, J. R.: Meteorological bias in satellite estimates of aerosol-cloud relationships, Geophys. Res. Lett., 34, L16824, doi:10.1029/2007GL029952, 2007.

Atmospheric
Chemistry
and Physics
Discussions

Open Access

EGU

McComiskey, A. and Feingold, G.: The scale problem in quantifying aerosol indirect effects, Atmos. Chem. Phys., 12, 1031–1049, https://doi.org/10.5194/acp-12-1031-2012, 2012.

1100   McFarquhar, G. M., Zhang, G., Poellot, M. R., Kok, G. L., McCoy, R., Tooman, T., Fridlind, A., and Heymsfield, A. J.: Ice properties of single-layer stratocumulus during the Mixed-Phase Arctic Cloud Experiment: 1. Observations, J. Geophys. Res., 112, D24201, doi:10.1029/2007jd008633, 2007.

McFarquhar, G. M., Finlon, J. A., Stechman, D. M., Wu, W., Jackson, R. C., and Freer, M.: University

1105   of Illinois/Oklahoma Optical Array Probe (OAP) Processing Software, https://doi.org/10.5281/zenodo.1285969, 2018.

Merk, D., Deneke, H., Pospichal, B., and Seifert, P.: Investigation of the adiabatic assumption for estimating cloud micro- and macrophysical properties from satellite and ground observations, Atmos. Chem. Phys., 16, 933–952, https://doi.org/10.5194/acp-16-933-

1110   2016, 2016.

Michibata, T., Suzuki, K., Sato, Y., and Takemura, T.: The source of discrepancies in aerosol–cloud–precipitation interactions between GCM and A-Train retrievals, Atmos. Chem. Phys., 16, 15413–15424, https://doi.org/10.5194/acp-16-15413-2016, 2016.

Min, Q., Joseph, E., Lin, Y., Min, L., Yin, B., Daum, P. H., Kleinman, L. I., Wang, J., and Lee, Y.-N.:

1115   Comparison of MODIS cloud microphysical properties with in-situ measurements over the Southeast Pacific, Atmos. Chem. Phys., 12, 11261–11273, https://doi.org/10.5194/acp-12-11261-2012, 2012.

Atmospheric
Chemistry
and Physics
Discussions

Morrison, H. and Gettelman, A.: A new two-moment bulk stratiform cloud microphysics scheme in the community atmosphere model, version 3 (CAM3). Part I: Description and numerical

1120   tests, J. Climate, 21, 3642–3659, doi:10.1175/2008JCLI2105.1, 2008.

ORACLES Science Team: Suite of Aerosol, Cloud, and Related Data Acquired Aboard P3 During ORACLES 2018, Version 2, NASA Ames Earth Science Project Office, https://doi.org/10.5067/Suborbital/ORACLES/P3/2018_V2, 2020a.

ORACLES Science Team: Suite of Aerosol, Cloud, and Related Data Acquired Aboard P3 During

1125   ORACLES 2017, Version 2, NASA Ames Earth Science Project Office, https://doi.org/10.5067/Suborbital/ORACLES/P3/2017_V2, 2020b.

ORACLES Science Team: Suite of Aerosol, Cloud, and Related Data Acquired Aboard P3 During ORACLES 2016, Version 2, NASA Ames Earth Science Project Office, https://doi.org/10.5067/Suborbital/ORACLES/P3/2016_V2, 2020c.

1130   Oreopoulos, L. and Rossow, W. B.: The cloud radiative effects of International Satellite Cloud Climatology Project weather states, J. Geophys. Res.-Atmos., 116, D12202, doi:10.1029/2010JD015472, 2011.

Painemal, D. and Zuidema, P.: Assessment of MODIS cloud effective radius and optical thickness retrievals over the Southeast Pacific with VOCALS-REx in situ measurements, J. Geophys.

1135   Res.-Atmos., 116, D24206, doi:10.1029/2011JD016155, 2011.

Pawlowska, H. and Brenguier, J. L.: An observational study of drizzle formation in stratocumulus clouds for general circulation model (GCM) parameterizations, J. Geophys. Res.-Atmos., 108, 8630, doi:10.1029/2002JD002679, 2003.

Penner, J. E., Quaas, J., Storelvmo, T., Takemura, T., Boucher, O., Guo, H., Kirkevåg, A.,

1140   Kristjánsson, J. E., and Seland, Ø.: Model intercomparison of indirect aerosol effects,

Atmos. Chem. Phys., 6, 3391–3405, https://doi.org/10.5194/acp-6-3391-2006, 2006.

Pistone, K., Redemann, J., Doherty, S., Zuidema, P., Burton, S., Cairns, B., Cochrane, S., Ferrare,

R., Flynn, C., Freitag, S., Howell, S. G., Kacenelenbogen, M., LeBlanc, S., Liu, X., Schmidt, K.

S., Sedlacek III, A. J., Segal-Rozenhaimer, M., Shinozuka, Y., Stamnes, S., van Diedenhoven,

1145   B., Van Harten, G., and Xu, F.: Intercomparison of biomass burning aerosol optical

properties from in situ and remote-sensing instruments in ORACLES-2016, Atmos. Chem.

Phys., 19, 9181–9208, https://doi.org/10.5194/acp-19-9181-2019, 2019.

Pistone, K., Zuidema, P., Wood, R., Diamond, M., da Silva, A. M., Ferrada, G., Saide, P., Ueyama,

R., Ryoo, J.-M., Pfister, L., Podolske, J., Noone, D., Bennett, R., Stith, E., Carmichael, G.,

1150   Redemann, J., Flynn, C., LeBlanc, S., Segal-Rozenhaimer, M., and Shinozuka, Y.: Exploring

the elevated water vapor signal associated with the free-tropospheric biomass burning

plume over the southeast Atlantic Ocean, Atmos. Chem. Phys. Discuss. [preprint],

https://doi.org/10.5194/acp-2020-1322, in review, 2021.

Platnick, S. and Twomey, S.: Determining the susceptibility of cloud albedo to changes in droplet

1155   concentration with the advanced very high resolution radiometer, J. Appl. Meteor., 33,

334–346, 1994.

Possner, A., Eastman, R., Bender, F., and Glassmeier, F.: Deconvolution of boundary layer depth

and aerosol constraints on cloud water path in subtropical stratocumulus decks, Atmos.

Chem. Phys., 20, 3609–3621, https://doi.org/10.5194/acp-20-3609-2020, 2020.

1160   Quaas, J., Arola, A., Cairns, B., Christensen, M., Deneke, H., Ekman, A. M. L., Feingold, G., Fridlind,
        A., Gryspeerdt, E., Hasekamp, O., Li, Z., Lipponen, A., Ma, P.-L., Mülmenstädt, J., Nenes,
        A., Penner, J. E., Rosenfeld, D., Schrödner, R., Sinclair, K., Sourdeval, O., Stier, P., Tesche,
        M., van Diedenhoven, B., and Wendisch, M.: Constraining the Twomey effect from
        satellite observations: issues and perspectives, Atmos. Chem. Phys., 20, 15079–15099,
1165   https://doi.org/10.5194/acp-20-15079-2020, 2020.

        Rao S., Dey S.: Consistent signal of aerosol indirect and semi-direct effect on water clouds in the
        oceanic regions adjacent to the Indian subcontinent. Atmos Res,
        232:104677. https://doi.org/10.1016/j.atmosres.2019.104677, 2020.

        Redemann, J., Wood, R., Zuidema, P., Doherty, S. J., Luna, B., LeBlanc, S. E., Diamond, M. S.,
1170   Shinozuka, Y., Chang, I. Y., Ueyama, R., Pfister, L., Ryoo, J.-M., Dobracki, A. N., da Silva, A.
        M., Longo, K. M., Kacenelenbogen, M. S., Flynn, C. J., Pistone, K., Knox, N. M., Piketh, S. J.,
        Haywood, J. M., Formenti, P., Mallet, M., Stier, P., Ackerman, A. S., Bauer, S. E., Fridlind,
        A. M., Carmichael, G. R., Saide, P. E., Ferrada, G. A., Howell, S. G., Freitag, S., Cairns, B.,
        Holben, B. N., Knobelspiesse, K. D., Tanelli, S., L'Ecuyer, T. S., Dzambo, A. M., Sy, O. O.,
1175   McFarquhar, G. M., Poellot, M. R., Gupta, S., O'Brien, J. R., Nenes, A., Kacarab, M., Wong,
        J. P. S., Small-Griswold, J. D., Thornhill, K. L., Noone, D., Podolske, J. R., Schmidt, K. S.,
        Pilewskie, P., Chen, H., Cochrane, S. P., Sedlacek, A. J., Lang, T. J., Stith, E., Segal-
        Rozenhaimer, M., Ferrare, R. A., Burton, S. P., Hostetler, C. A., Diner, D. J., Seidel, F. C.,
        Platnick, S. E., Myers, J. S., Meyer, K. G., Spangenberg, D. A., Maring, H., and Gao, L.: An
1180   overview of the ORACLES (ObseRvations of Aerosols above CLouds and their intEractionS)

project: aerosol–cloud–radiation interactions in the southeast Atlantic basin, Atmos. Chem. Phys., 21, 1507–1563, https://doi.org/10.5194/acp-21-1507-2021, 2021.

Rogers, R. R. and Yau, M. K.: A Short Course in Cloud Physics, 3rd Edn., International Series in Natural Philosophy, 290 pp., 1989.

1185   Small, J. D., Chuang, P. Y., Feingold, G., and Jiang, H.: Can aerosol decrease cloud lifetime?, Geophys. Res. Lett., 36, 16806, doi:10.1029/2009GL038888, 2009.

Sakaeda, N., Wood, R., and Rasch, P. J.: Direct and semidirect aerosol effects of southern African biomass burning aerosol, J. Geophys. Res., 116, D12205, doi:10.1029/2010JD015540, 2011.

1190   Sorooshian, A., Anderson, B., Bauer, S. E., Braun, R. A., Cairns, B., Crosbie, E., Dadashazar, H., Diskin, G., Ferrare, R., Flagan, R. C., Hair, J., Hostetler, C., Jonsson, H. H., Kleb, M. M., Liu, H. Y., MacDonald, A. B., McComiskey, A., Moore, R., Painemal, D., Russell, L. M., Seinfeld, J. H., Shook, M., Smith, W. L., Thornhill, K., Tselioudis, G., Wang, H. L., Zeng, X. B., Zhang, B., Ziemba, L., and Zuidema, P.: Aerosol-Cloud-Meteorology Interaction Airborne Field

1195   Investigations: Using Lessons Learned from the US West Coast in the Design of ACTIVATE off the US East Coast, B. Am. Meteorol. Soc., 100, 1511–1528, https://doi.org/10.1175/Bams-D-18-0100.1, 2019.

Sorooshian, A., Feingold, G., Lebsock, M. D., Jiang, H., and Stephens, G. L.: On the precipitation susceptibility of clouds to aerosol perturbations, Geophys. Res. Lett., 36, L13803,

1200   doi:10.1029/2009GL038993, 2009.

Sorooshian, A., Feingold, G., Lebsock, M. D., Jiang, H., and Stephens, G.: Deconstructing the precipitation susceptibility construct: improving methodology for aerosol cloud precipitation studies, J. Geophys. Res., 115, D17201, doi:10.1029/2009JD013426, 2010.

Stephens, G. L., L'Ecuyer, T., Forbes, R., Gettlemen, A., Golaz, J. C., Bodas-Salcedo, A., Suzuki, K., Gabriel, P., and Haynes, J.: Dreary state of precipitation in global models, J. Geophys. Res.-Atmos., 115, D24211, doi:10.1029/2010jd014532, 2010.

Stevens, B. and Feingold, G.: Untangling aerosol effects on clouds and precipitation in a buffered system, Nature, 461, 607–613, doi:10.1038/nature08281, 2009.

Terai, C. R., Wood, R., Leon, D. C., and Zuidema, P.: Does precipitation susceptibility vary with increasing cloud thickness in marine stratocumulus?, Atmos. Chem. Phys., 12, 4567–4583, doi:10.5194/acp-12-4567-2012, 2012.

Toll, V., Christensen, M., Quaas, J., and Bellouin, N.: Weak average liquid-cloud-water response to anthropogenic aerosols, Nature, 572, 51–55, https://doi.org/10.1038/s41586-019-1423-9, 2019.

Trenberth, K. and Fasullo, J.: Global warming due to increasing absorbed solar radiation, Geophys. Res. Lett., 36, L07706, doi:10.1029/2009GL037527, 2009.

Twomey, S.: Pollution and the Planetary Albedo, Atmos. Environ., 8, 1251–1256, 1974.

Twomey, S.: The influence of pollution on the shortwave albedo of clouds. J. Atmos. Sci., 34, 1149-1152, 1977.

Weigel, R., Spichtinger, P., Mahnke, C., Klingebiel, M., Afchine, A., Petzold, A., Krämer, M., Costa, A., Molleker, S., Reutter, P., Szakáll, M., Port, M., Grulich, L., Jurkat, T., Minikin, A., and Borrmann, S.: Thermodynamic correction of particle concentrations measured by

1205

1210

1215

1220

underwing probes on fast-flying aircraft, Atmos. Meas. Tech., 9, 5135–5162, https://doi.org/10.5194/amt-9-5135-2016, 2016.

1225 Wilcox, E. M.: Stratocumulus cloud thickening beneath layers of absorbing smoke aerosol, Atmos. Chem. Phys., 10, 11769–11777, https://doi.org/10.5194/acp-10-11769-2010, 2010.

Wood, R. and Hartmann, D. L.: Spatial variability of liquid water path in marine low cloud: the importance of mesoscale cellular convection, J. Climate, 19, 1748–1764, 2006.

Wood, R., Kubar, T. L., and Hartmann, D. L.: Understanding the Importance of Microphysics and
1230 Macrophysics for Warm Rain in Marine Low Clouds. Part II: Heuristic Models of Rain Formation, J. Atmos. Sci., 66, 2973–2990, doi:10.1175/2009JAS3072.1, 2009.

Wood, R.: Stratocumulus Clouds, Mon. Weather Rev., 140, 2373–2423, doi:10.1175/MWR-D-11-00121.1, 2012.

Xue, H. and Feingold, G.: Large eddy simulations of trade wind cumuli: investigation of aerosol
1235 indirect effects, J. Atmos. Sci., 63, 1605–1622, 2006.

Zhang, Z. and Platnick, S.: An assessment of differences between cloud effective particle radius retrievals for marine water clouds from three MODIS spectral bands, J. Geophys. Res.-Atmos., 116, D20215, doi:10.1029/2011JD016216, 2011.

Zuidema, P., Redemann, J., Haywood, J., Wood, R., Piketh, S., Hipondoka, M. and Formenti, P.:
1240 Smoke and Clouds above the Southeast Atlantic: Upcoming Field Campaigns Probe Absorbing Aerosol's Impact on Climate, Bull. Am. Meteorol. Soc., 160129100143006, doi:10.1175/BAMS-D-15-00082.1, 2016.